D.A. Dei Tos, R.P. Russell, F. Topputo
Survey of Mars Ballistic Capture Trajectories Using Periodic Orbits as Generating Mechanisms
Journal of Guidance Control and Dynamics, Vol. 41, N. 6, 2018, p. 1227-1242
doi:10.2514/1.G003158

Survey of Mars ballistic capture trajectories using periodic orbits as generating mechanisms

Diogene A. Dei Tos[1]
Politecnico di Milano, 20156 Milan, Italy

Ryan P. Russell[2]
University of Texas at Austin, Austin, Texas 78712

Francesco Topputo[3]
Politecnico di Milano, 20156 Milan, Italy

A systematic approach is devised to find ballistic captures in the planar elliptic restricted three-body problem. Simple symmetric periodic orbits around the smaller primary in the circular problem are used as generators for ballistic captures. Combining a scaling factor that maps states from the circular to the elliptic model, and restricting the motion to emanate from periodic solutions, the search space for ballistic capture is reduced to three dimensions. Results in the Sun–Mars system indicate an abundance of long-duration, regular solutions with a variety of characteristics, including low osculating eccentricities. A large scale survey is completed using 3 families of periodic orbits encompassing more than 2,600 periodic solutions. Discretizing over the mapping parameter, the Mars true anomaly, and the generating periodic orbits, 37 million ballistic captures are evaluated and classified for potential use. The existence of sample solutions into a high-fidelity ephemeris model is evidenced.

---

[1]Ph.D. Candidate, Department of Aerospace Science and Technology; diogenealessandro.deitos@polimi.it.

[2]Associate Professor, Department of Aerospace Engineering and Engineering Mechanics; ryan.russell@utexas.edu. Associate Fellow AIAA.

[3]Assistant Professor, Department of Aerospace Science and Technology; francesco.topputo@polimi.it. Member AIAA.

Nomenclature

C	=	Rotation matrix	[-]
$\mathcal{C}$	=	Ballistic capture set	[-]
$\mathcal{E}$	=	Escape set	[-]
e_0	=	Initial osculating eccentricity	[-]
e_p	=	Primaries eccentricity	[-]
f	=	True anomaly of the smaller primary	[deg]
H_2	=	Kepler energy with respect to the smaller primary	[km/s^2]
$I_{\sigma\times\sigma}$	=	σ by σ identity matrix, where $\sigma \in \mathbb{Z}_+$	[-]
J	=	Jacobi constant	[-]
k	=	Map parameter	[-]
$\mathcal{K}$	=	Crash set	[-]
k_1	=	Stability index	[-]
$m_{1,2,3}$	=	Mass of $P_{1,2,3}$	[kg]
M	=	Monodromy matrix	[-]
n_f	=	Grid dimension of true anomaly	[-]
n_k	=	Grid dimension of map parameter	[-]
N_r	=	Number of P_3 revolutions about P_2	[-]
N_s	=	Number of solutions	[-]
$N_s^{\mathcal{C}}$	=	Capture ratio	[-]
N_x	=	Number of x axis crossings	[-]
$\mathcal{P}$	=	Persistent set	[-]
p_0	=	Initial osculating semi-latus rectum	[km]
$P_{1,2,3}$	=	Smaller primary, larger primary, and artificial object	[-]
$\boldsymbol{R}$	=	Inertial P_2-centered position vector	[km]
r_0	=	Initial osculating pericenter radius	[-]
$\boldsymbol{r}_2$	=	Synodic position vector with respect to P_2	[-]
r_p	=	Primaries distance	[km]
R_s	=	Mars sphere of influence	[km]
$R_{\male}$	=	Mars mean radius	[km]
S	=	Regularity index	[-]
T	=	Orbital period in the synodic frame	[-]
$\boldsymbol{V}$	=	Inertial P_2-centered velocity vector	[km/s]
$\boldsymbol{v}_2$	=	Synodic velocity vector with respect to P_2	[-]
$\mathcal{W}$	=	Weakly stable set	[-]
μ_2	=	Mars gravitational parameter	[km^3/s^2]
$\Delta S_{\%}$	=	Regularity coefficient	[-]
ι	=	Percentile threshold	[-]
λ_1	=	First eigenvalue of monodromy matrix	[-]
ω	=	Pseudo-potential of the elliptic problem	[-]

Subscripts

$(\cdot)_0$	=	Initial condition
$(\cdot)_2$	=	Quantity with respect to P_2
$(\cdot)_e$	=	Escape
$(\cdot)_k$	=	Crash
$(\cdot)_r$	=	Revolution

Superscripts

$(\cdot)^+$	=	Forward integration
$(\cdot)^-$	=	Backward integration
$(\cdot)^{(2b)}$	=	Kepler two-body quantity
$(\cdot)^{(c)}$	=	Circular restricted three-body problem quantity
$(\cdot)^{(j)}$	=	Looping index

I. Introduction

Low-energy transfers, of which ballistic capture is an important mechanism, have gained central importance in space mission analysis and design. These orbits provide improved mission versatility when compared to Keplerian solutions. In fact, ballistic capture is used in astrodynamics to reduce fuel consumption [1], mitigate the risks associated to single-point burn failures [2], and accommodate wider launch windows [3, 4]. These advantages are achieved at the cost of generally longer transfer times [5, 6]. Ballistic capture enabled the rescue of Hiten [7], and was used in SMART-1 [8] and GRAIL [9] missions. It has been proposed in BepiColombo [2], Lunette [10], and ESMO [11]. The applicability of ballistic capture in asteroid retrieval contexts has also been analyzed [12].

The concept of ballistic capture is intimately related to that of weak stability boundary (WSB), heuristically proposed in the context of an Earth-to-Moon transfer [13]. The goal was to produce trajectories in which the spacecraft approaches the Moon and temporarily revolves about it in a totally natural fashion. However, since then, several distinct definitions share the WSB and ballistic capture nomenclature. Originally, (a) the design strategy of low-energy transfers was associated to a fuzzy boundary region located at approximately 1.5 million km away from the Earth in the Sun–Earth direction [14]. (b) An algorithmic definition for the WSB had since been proposed [15], and later reviewed and extended [16], based on the classification of sets of osculating initial conditions around the smaller primary. These sets give rise to orbits satisfying a simple definition of stability [17, 18], based on prescribed energetic and geometric behavior. (c) The WSB has also been interpreted as the intersection of three subsets of the phase space [19, 20], and d) has been derived from weakly stable sets and escape sets, whose intersection forms capture sets at specified osculating parameters [21].

Ballistic capture orbits have been studied in the Hill problem [22], the planar [4, 23] and spatial [24] circular restricted three-body problem (CRTBP), incorporating planet eccentricity [21, 25–29], the effect of perturbations [30], and in the full-ephemeris dynamics [31–35]. Although some light was shed in the above-mentioned works, the global picture behind the ballistic capture mechanism is yet to be thoroughly understood. As dynamical models become nonautonomous or nonconservative, the

lack of invariant structures requires leveraging the dynamical insight to reduce the complexity of the analysis and explore the whole extent of a six-dimensional space. Solutions are not scalable and do not provide a deeper understanding of the complex dynamics at hand. These issues, coupled with the high sensitivity to initial conditions, have limited the use of ballistic captures in applied mission designs. On the other hand, few works have tried to establish a connection between the WSBs and the CRTBP periodic orbits, limiting the research to Lagrange point dynamics [16, 36, 37]. Periodic solutions represent a resource to describe and quantify the dynamics in the neighborhood of the smaller primary, in terms of orbit size, period, energy, altitude profiles, and stability properties [38–42]. The chaotic and stability features of the CRTBP are so marked that their effects reverberate when extended to higher fidelity models [43, 44]. An example is the persistency of large stability islands, seen in a Poincaré map, associated to distant retrograde orbits (DROs) [45]. The phase space of the CRTBP has been already demonstrated to be the backbone for several mechanisms in nonautonomous and nonconservative models [46–48]. Accordingly, evidence is mounting that the ballistic capture mechanism is intimately related to CRTBP periodic solutions.

The main objective of this work is to find conditions that generate weakly capture orbits in the elliptic restricted three-body problem (ERTBP). In the circular problem, periodic orbits (POs) and their stable and unstable manifolds provide sufficient dynamical diversity to span most of the CRTBP phase space. This convenient property is not true for the elliptic case. Symmetric POs exist in the planar ERTBP only for a discrete sets of primary geometrical configurations (e. g., with initial true anomalies that are exact multiple of π), otherwise quasi-periodic motion is obtained [49]. In [17, 28], finding planar ballistic captures require fine searching through a $4D$ search space. However, alternative approaches may rely on manifold-type structures (analogous to invariant manifolds in the CRTBP) and Lagrangian coherent structures can be computed in the ERTBP [50, 51], and could involve corrections of known periodic and quasi-periodic solutions to recover trajectories with long-term stability properties [49].

In this paper, the use of a single-parameter mapping is proposed to make up for the lack of manifolds and to link the circular and elliptic problems. Periodic orbits of the circular problem, computed

through a global grid search and differential correction [40], are mapped to states in the ERTBP, which then constitute the initial conditions for ballistic captures. This mapping is applied for the first time in the Sun–Mars context (case study of this work), but has proved useful in the continuation from the Jupiter–Europa CRTBP to the ephemeris model [52]. By restricting to motion that emanates from periodic solutions in the CRTBP, the $4D$ search space is reduced to $3D$. Moreover, thanks to the symmetric nature of the CRTBP, candidate initial conditions in the elliptic problem always start at the periapsis of an osculating conic about the smaller primary, compatibly with the algorithmic definition of WSB. The use of CRTBP periodic orbits as generators for ballistic captures in the elliptic problem, and the mapping approach, is motivated for systems with low (but not negligible) eccentricities; e. g., Sun–Mars. The method devised in this work exploits the transport mechanism of POs when transitioning from the circular to the elliptic model. To large deviations from the CRTBP assumptions (e. g., highly elliptical motion of primaries) correspond large deviations on the transport mechanism during the transition, and hence a variation in performance for the search of ballistic captures.

The remainder is organized as follows. Dynamical models are described in the following Section. Next, the methodology is briefly reviewed to seek planar CRTBP periodic orbits. Periodic initial conditions are mapped to the elliptic problem, then solutions are placed into proper sets. The definition of ballistic capture is applied and the algorithm to construct weakly captured solutions from periodic orbits is presented. The Results Section elaborates on POs and the resulting ballistic captures. Samples of regular and irregular trajectories are shown and recommendations for an applied context are given according to the global behavior of the ballistic capture solutions. Families and stability indices of periodic solutions are connected to the quantity and quality of the resulting ballistic capture orbits. Finally, sample ballistic captures in a high-fidelity model are shown and conclusions are drawn.

II. Dynamical models

A. The planar circular restricted three-body problem

Let us consider a body P_3 of mass m_3 in the vector field of a larger primary, P_1, and a smaller primary, P_2, of masses m_1 and m_2, respectively, such that the condition $m_3 \ll m_2 < m_1$ is satisfied. The primaries revolve in planar configuration at constant angular speed. The motion of the third body, or particle, is studied in a rotating synodic reference frame, whose origin is located at the primaries center of mass, the x axis is always aligned with the P_1P_2 direction, the z axis is orthogonal to their plane of motion, and the y axis forms a right-hand tern. By means of a proper nondimensionalization [53] the equations of motion depend only on the mass parameter, defined as $\mu = m_2/(m_1 + m_2)$. The nondimensionalization is such that the distance between the primaries, their angular speed, and the sum of their masses are set to a unity value. The equations for the motion of P_3 are

$$\dot{\boldsymbol{x}}^{(c)} = \boldsymbol{f}(\boldsymbol{x}^{(c)}) := \left(u^{(c)}, v^{(c)}, 2v^{(c)} + \Omega_{/x^{(c)}}, -2u^{(c)} + \Omega_{/y^{(c)}}\right)^{\mathrm{T}}, \tag{1}$$

where $\boldsymbol{x}^{(c)} := (x^{(c)}, y^{(c)}, u^{(c)}, v^{(c)})^{\mathrm{T}}$ is P_3 state, dots denote derivatives with respect to nondimensional time, and slashed subscripts are partial derivatives. The three-body pseudo-potential is

$$\Omega = \frac{1}{2}\left[(x^{(c)})^2 + (y^{(c)})^2\right] + \frac{1-\mu}{r_1} + \frac{\mu}{r_2} + \frac{1}{2}\mu(1-\mu), \tag{2}$$

where terms $r_1 = \sqrt{(x^{(c)} + \mu)^2 + (y^{(c)})^2}$ and $r_2 = \sqrt{(x^{(c)} - 1 + \mu)^2 + (y^{(c)})^2}$ are the distances between P_3 and each primary, respectively. Because the system is Hamiltonian and autonomous, an integral of motion exists, i. e., the Jacobi constant:

$$J(x^{(c)}, y^{(c)}, u^{(c)}, v^{(c)}) := 2\Omega(x^{(c)}, y^{(c)}) - \left[(u^{(c)})^2 + (v^{(c)})^2\right]. \tag{3}$$

The CRTBP possesses five equilibrium points, three of them located along the x axis (collinear points $L_{1,2,3}$), and the others at the vertex of two equilateral triangles having the primaries distance as common base (triangular points $L_{4,5}$). These points are also referred as Lagrangian or libration

points. The state transition matrix (STM), $\Phi(t_0,t) = \left[\dfrac{\partial \boldsymbol{x}^{(c)}(t)}{\partial \boldsymbol{x}^{(c)}(t_0)}\right]$, is obtained by integrating the variational equations

$$\dot{\Phi}(t_0,t) = \left[\frac{\partial \boldsymbol{f}}{\partial \boldsymbol{x}^{(c)}}\right]\Phi(t_0,t), \qquad \Phi(t_0,t_0) = I_{4\times 4}, \tag{4}$$

from t_0 to t. The STM plays an important role in determining the stability of a periodic orbit. It is an essential part for the differential correction scheme used for the investigation carried out in this work, which relies on the derivatives of a final state with respect to a given initial state. The first order time-free variation of a reference solution $\boldsymbol{x}^{(c)}(t)$ reads

$$\delta \boldsymbol{x}^{(c)}(t+\delta t) = \Phi(t_0,t)\delta \boldsymbol{x}^{(c)}(t_0) + \dot{\boldsymbol{x}}^{(c)}(t)\delta t. \tag{5}$$

B. The planar elliptic restricted three-body problem

In the elliptic restricted three-body problem both primaries move on elliptic orbits of common eccentricity, e_p. Let f be the true anomaly of P_2, the equations for the planar motion of P_3 are [53]

$$x'' - 2y' = \omega_{/x}, \qquad y'' + 2x' = \omega_{/y}, \tag{6}$$

where primes denote derivatives with respect to f, and the elliptic pseudo-potential is

$$\omega(x,y,f) = \frac{\Omega}{1+e_p\cos f}, \tag{7}$$

in which Ω is the one defined in Eq. (2). Eqs. (6) are written in a nonuniformly rotating, barycentric, nondimensional coordinate frame. The coordinate frame isotropically pulsates as the P_1P_2 distance is assumed to be the unit length. The independent variable plays the role of time: f is zero when P_1, P_2 are at their periapsis. Normalizing the period of the primaries to 2π, the dependence of f on nondimensional time is

$$\frac{\mathrm{d}f}{\mathrm{d}t} = \frac{(1+e_p\cos f)^2}{(1-e_p)^{3/2}}. \tag{8}$$

Table 1: Parameters of the Sun–Mars system.

Parameter	Symbol	Value
Mass ratio	μ	$3.227154876045166 \times 10^{-6}$
Length unit	LU	$2.279497905330276 \times 10^{8}$ km
Time unit	TU	109.3425420965616 days
Velocity unit	VU	24.128831378998047 km/s
Eccentricity	e_p	0.0935643512
Mars mean radius	$R_{\mathord{\male}}$	3396.19 km
Mars sphere of influence	R_s	577254.3 km
Mars gravitational parameter	μ_2	4282.837362069909 $\mathrm{km}^3/\mathrm{s}^2$
Interior Lagrangian point location with respect to Mars	x_{L_1}	$-1.082385474 \times 10^{6}$ km
Exterior Lagrangian point location with respect to Mars	x_{L_2}	$1.085822733 \times 10^{6}$ km

Unlike the CRTBP, the true anomaly in Eq. (7) makes the elliptic problem nonautonomous. The trajectory-dependent integral of motion of the elliptic problem reads

$$\hat{J}(x, y, u, v, f) := 2\omega(x, y) - (u^2 + v^2) - 2e_p \int_{f_0}^{f} \frac{\Omega(x, y) \sin \tilde{f}}{(1 + e_p \cos \tilde{f})^2} \mathrm{d}\tilde{f}. \tag{9}$$

Once the energy level is specified, Eq. (9) defines allowed and forbidden regions of motion, bounded by pulsating Hill curves. These curves vary according to the mutual position of the primaries. Table 1 gives SPICE[1] estimates for the mean Sun–Mars parameters used in this work. Ephemeris file *de432s* is used, and Mars orbital elements are computed by means of a time average.

III. Periodic orbits

Closely following the approach in Russell (2006) [40], periodic orbits around P_2 in the planar CRTBP are computed by (1) making explicit use of restricted three-body problem symmetries, (2) targeting the periodicity condition via a local differential correction, and (3) implementing a numerical exploration for the grid search parameters. Based on the propagation of deviations from a reference state (i. e., Eq. (5)), the differential correction is a single shooting that tweaks the initial vertical velocity $v_0^{(c)}$, and the nondimensional PO period, T, once the initial horizontal position, $x_0^{(c)}$, is fixed, in order to obtain trajectories with two perpendicular x axis crossings separated by $T/2$ time

[1]The toolkit is freely available through the NASA NAIF website; refer to `http://naif.jpl.nasa.gov/naif/`. Downloaded on Dec 22, 2016.

units (see [40] for more details). At both perpendicular crossings, $y^{(c)} = u^{(c)} = 0$. The stability of a periodic orbit depends on the spectrum of its monodromy matrix (the STM evaluated after one period), $M := \Phi(0, T)$. The monodromy matrix provides a linear mapping of small initial state perturbations across a full period (refer to Eq. (5)). Because of the symplectic nature of Φ matrix [54], the eigenvalues of M occur in reciprocal pairs. There are two unity eigenvalues due to the existence of the Jacobi constant and to the exact periodicity of the solution. The eigenvalues of M in the planar CRTBP thus occur as $(\lambda_1, 1/\lambda_1, 1, 1)$. If an eigendirection exists that leads to a contraction, then there is also an accompanying eigendirection that leads to an expansion. A common way to indicate stability is the *stability index*, $k_1 = |\lambda_1 + 1/\lambda_1|$ [40, 54]. A periodic solution in the CRTBP is termed

1. *Stable* if $k_1 \leq 2$; 2. *Mildly unstable* if $k_1 \in (2, 11]$; 3. *Unstable* if $k_1 > 11$.

For the classification of stability, $|\cdot|$ represents the Euclidean norm of a complex number. Stability index $k_1 = 11$ is a convenient threshold found with numerical experiments that is used in this work to differentiate stability properties of periodic solutions. This value is chosen to have the size of periodic orbit families uniformly distributed across the stability index. Observation for a particular subset of parameters in transitioning from the CRTBP to the ERTBP has shown that k_1 is also a good indicator of persistence (see Definition 4 in Section IV C) for the solutions mapped into the elliptic problem. Periodic initial conditions are grouped according to their stability indices and relations with the WSBs are sought for these groups.

IV. Ballistic capture

A. Initial conditions set

In the planar elliptic problem, an initial condition is specified by 5 scalars, which define the spacecraft position, $\boldsymbol{r}_0 = (x_0, y_0)^{\mathrm{T}}$, and velocity, $\boldsymbol{v}_0 = (u_0, v_0)^{\mathrm{T}}$, for a given value of true anomaly, f_0. Let $l(\vartheta)$ be the radial segment emanating from the smaller primary and connecting P_2 with P_3, where ϑ is the counterclockwise angle measured from the x axis to $l(\vartheta)$. According to the algorithmic definition of WSBs [15], sets of initial conditions are constructed for which P_3 departs from $l(\vartheta)$ while being

at the pericenter of an osculating ellipse around P_2 with eccentricity e_0 and radius r_0. In this case, the search space variables are $(r_0, \vartheta, e_0, f_0)$. These initial conditions are then propagated forward and backward in the ERTBP. Ballistic captures are classified according to energetic and geometric criteria. Correlations between the osculating orbital parameters and the quantity and quality of the weakly captured solutions have been found [21]. The role of system true anomaly in the ballistic capture process has also been investigated [28]. Boundaries for the problem variables can be derived from these correlations, thus reducing the search space size. Nevertheless, ballistic capture solutions in the planar ERTBP are found by sampling a four-dimensional space.

In the present work, a different approach altogether is pursued: periodic orbits around P_2 within the CRTBP constitute the sets of initial conditions for the computation of weakly captured solutions in the elliptic problem. The idea is that periodicity is a persistent property of the CRTBP phase space and plays an important role also in the ERTBP. Under specific conditions, stable, mildly unstable, and unstable periodic orbits can generate, when integrated in the elliptic problem, trajectories that temporarily orbit around P_2 in a weakly captured state, or quickly escape from it. These properties are essentially the same mechanisms that enable weakly captured motion. Numerical simulations show that ballistic capture solutions exist starting from simple symmetric periodic orbits (i. e., one revolution in the synodic frame around the smaller primary) with a wide range of k_1.

As an example, in Fig. 1 six initial conditions corresponding to periodic solutions of the CRTBP are propagated in the ERTBP, from $f_0 = 0$ to twice the period of the generating periodic orbit. Ordered by columns, there are 2 stable, 2 mildly unstable, and 2 unstable periodic orbits, respectively. Their integration in the elliptic problem gives rise to both bounded (first row, see Definition 1 in Section IV C), and unbounded motion (second row). In the latter scenario, the zero-velocity curves (ZVCs) of the elliptic problem allow P_3 to escape following a path that would have been prohibited in the CRTBP. The ZVCs, dashed lines in Fig. 1, correspond to the Jacobi constant of the CRTBP periodic orbit.

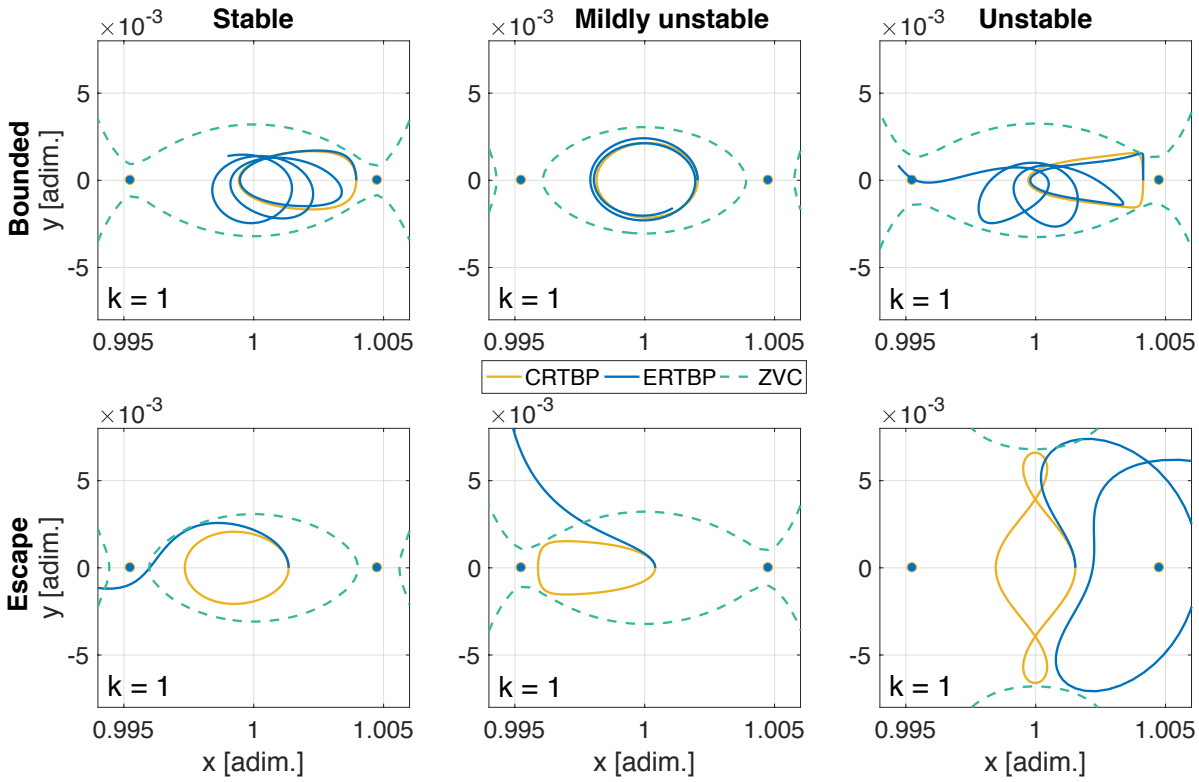

Fig. 1: Trajectories of periodic initial conditions in the CRTBP (light line), and their ERTBP propagation (dark line). (See Eq. (10) for the meaning of k.)

B. Single-parameter mapping

The transformation between the circular and elliptic problems is yet another important variable for seeking ballistic capture solutions. Let $\boldsymbol{x}_0^{(c)} = (x_0^{(c)}, 0, 0, v_0^{(c)})^{\mathrm{T}}$ be the initial condition for a given periodic solution in the CRTBP, and let $\boldsymbol{x}_0 = (x_0, 0, 0, v_0)^{\mathrm{T}}$ be the corresponding initial condition in the ERTBP. A one-parameter map is introduced, $\mathcal{F}(k) : \boldsymbol{x}_0^{(c)} \to \boldsymbol{x}_0$, such that

$$x_0 = x_0^{(c)}, \qquad v_0 = \frac{v_0^{(c)}}{k}, \tag{10}$$

where k is the mapping parameter. This single-parameter mapping is simple, yet it introduces a degree of freedom to account for the pulsating nature of the elliptic problem. The sets of periodic orbits, represented by the initial conditions $(x_0^{(c)}, v_0^{(c)}, T)$, start on the x axis. The ERTBP position along the x axis is kept unchanged and equal to the CRTBP position. This approach preserves the x direction discretization of the periodic orbits (generally a subset of the grid used to compute the

POs). Bounds for the parameter k are heuristically found by means of a direct comparison between the circular and elliptic problems dynamics: the velocity transformation between the two systems yields $x' = \dot{x}/\dot{f}$. The true anomaly derivative with respect to time is then formally equivalent to the dynamical mapping parameter, $k \sim \dot{f}$. Eq. (8) provides a lower and upper bound for the map parameter given a P_1P_2 eccentricity ($k_{\min} = 0.95207$ and $k_{\max} = 1.38574$ for the Sun–Mars case), corresponding to values of true anomaly of $f = \pi$ and $f = 0$, respectively. In transitioning from the circular to the elliptic problem, the mapping parameter is allowed to vary between $k_{\min}$ and $k_{\max}$ to aid the transition from circular to elliptic problem and to ensure sufficient variety in the capture and escape trajectories produced in the ERTBP. A map approach is employed, instead of using discrete states along the PO as variables for the grid search, because the mapped initial state of a periodic orbit always lies at the periapsis of an osculating conic having one focus at P_2. In view of the properties of the map $\mathcal{F}(k)$, if velocity and position vectors are perpendicular in the CRTBP, then this property is true also after the mapping. Thus, the particle stays at osculating periapsis condition in the ERTBP, albeit with different osculating eccentricity and semi-latus rectum. Consequently, the search space is reduced and ballistic captures computed in this work may be compared to results of existing works that employ, for instance, the algorithmic definition of WSB [17, 31]. It is noted here that this mapping is simply a heuristic guided by intuition to allow a single parameter degree of freedom to the nontrivial mapping problem. Bounding k is also needed to proceed with a grid search.

ERTBP propagations are attached to a given value of system true anomaly. Hence, the quality and quantity of the ballistic capture solutions depend on the initial periodic state $x_0^{(c)}$, the initial system true anomaly f_0, and the map parameter k. Thus, the search space is three-dimensional, $(x_0^{(c)}, f_0, k)$; as opposed to the four-dimensional search space of the algorithmic WSB definition [15–18]. This reduction in search space is an improvement in terms of computational efficiency in comparison to an unguided grid search and for results interpretation. The stated improvement is not compared to other methods such as the quasi-periodic approach. For a given initial state in the circular problem (ascending x axis crossing of a periodic orbit), ballistic capture trajectories are sought by sampling (k, f_0). Let $\boldsymbol{x}_0 = (\boldsymbol{r}_0, \boldsymbol{v}_0)$ be the k-dependent initial condition in the ERTBP. Eqs. (6) are integrated

to yield $\boldsymbol{x}(f) = (\boldsymbol{r}(f), \boldsymbol{v}(f))$ for $f \in [f_0, f_0 \pm \Delta f_{\max}]$, where $\Delta f_{\max}$ is a maximum duration, and the plus/minus sign accounts for forward/backward integration. Analyzing only those solutions whose periapsis lies on the x axis, without spanning the full phase space around P_2, might seem a restrictive choice. However, this is just a by-product of how simple symmetric POs are defined. Furthermore, assuming that ballistic capture features quasi-regular motion, the solutions are simply ellipses in the inertial frame that circulate in argument of periapsis. Thus, these orbits eventually have their periapsis on or close to the x axis.

C. Criteria for orbits classification

For the planar case, the persistence (proxy for stability quality of a ballistic capture) of P_3 can be inferred by studying its intersections with the x axis. Let $\boldsymbol{x} = (x, y, u, v)^{\mathrm{T}}$ be a generic state of P_3 in the planar ERTBP.

Definition 1 (Revolution). *The particle performs a complete revolution around P_2 at true anomaly f_r if the following conditions are all simultaneously satisfied [35],*

$$i)\ y^{(j)}(f_r) = 0, \qquad ii)\ [x^{(j)}(f_r) - 1 + \mu](\bar{x} - 1 + \mu) > 0, \qquad iii)\ v^{(j)}(f_r)\bar{v} > 0, \tag{11}$$

where the superscript (j) counts the number of x axis crossings.

The first of Eqs. (11) expresses the particle intersection with the x axis at true anomaly f_r; the second condition limits the analysis to the segment of interest and excludes half revolutions; and the last kinematic condition is used to filter out undesired incomplete revolutions for which condi-

Algorithm 1 Algorithm to compute and update barred quantities in Definition 1.

Require: Initialize $\bar{x} = x^{(0)}$, $\bar{v} = v^{(0)}$, and number of revolutions, $N_r = 0$
for $j \leftarrow 1, N_x$ **do**
  Compute next x crossing with Condition i) of Eq. (11) and store $(x^{(j)}, v^{(j)})$
  if Condition ii) of Eq. (11) is satisfied **then**
    if Condition iii) of Eq. (11) is satisfied **then**
      Complete revolution around P_2 is counted, $N_r = N_r + 1$
    end if
    Update barred quantities, $\bar{x} = x^{(j)}$ and $\bar{v} = v^{(j)}$
  end if
end for

tion 1 and 2 are satisfied (e. g., two consecutive crossings on the same axis). Barred quantities in Eq. (1) indicate states on a preceding crossing ($j-1,\ldots,0$); they are updated with Algorithm 1. Updating the position and velocity as the particle moves along its trajectory is a modified version of conditions used in Luo et al. (2014) [31], for which some orbits were pruned out due to a restrictive kinematic constraint. Algorithm 1 cannot capture revolutions when P_3 motion becomes prograde from retrograde, and vice versa.

The Kepler specific mechanical energy of P_3 with respect to P_2 is

$$H_2 = \frac{\|\boldsymbol{V}\|^2}{2} - \frac{\mu_2}{\|\boldsymbol{R}\|}, \tag{12}$$

where

$$\boldsymbol{R} = r_p C \boldsymbol{r}_2, \qquad \boldsymbol{V} = \frac{\dot{f}}{TU}\left[(r_p' C + r_p C')\boldsymbol{r}_2 + r_p C \boldsymbol{v}_2\right], \tag{13}$$

and

$$C = \begin{bmatrix} \cos f & -\sin f \\ \sin f & \cos f \end{bmatrix}. \tag{14}$$

In Eqs. (12)–(13), μ_2 is the gravitational parameter of P_2 (see Table 1), $\boldsymbol{R}$ and $\boldsymbol{V}$ are P_3 position and velocity vectors in the inertial P_2-centered reference frame, respectively, $r_p(f) = LU(1-e_p^2)/(1+e_p\cos f)$ is the pulsating distance between the primaries, C is the rotation matrix, and $\boldsymbol{r}_2$, $\boldsymbol{v}_2$ are P_3 synodic position and velocity with respect to P_2, respectively.

Definition 2 (Escape). *The particle escapes from P_2 at true anomaly f_e if the following conditions are both satisfied [32],*

$$H_2(f_e) > 0, \qquad r(f_e) > R_s, \tag{15}$$

where H_2 is the Kepler energy as in Eq. (12)*, and R_s is the radius of P_2 sphere of influence (Table 1).*

According to Eq. (15), escape occurs when the particle is physically located outside of the P_2 sphere of influence (SOI) and, at the same time, it possesses positive Kepler energy with respect to P_2. The two conditions have to be satisfied simultaneously since the first one alone does not guarantee escape, and vice versa [17]. The Kepler specific mechanical energy in a multi-body environment is a fluctuating term and lacks the direct physical significance it has in the two-body problem. However, it has been shown that use of both geometrical and energetic conditions in Definition 2 is a conservative choice to discriminate between escape and weakly stable conditions [1, 17, 31]. The use of the sphere of influence to define escape in the multi-body dynamical system, rather than the $L_{1,2}$ gateways, is motivated by the wide energy level range of the present analysis.

Definition 3 (Crash). *Let $R_{\male}$ be P_2 mean radius (see Table 1), the particle impacts P_2 at true anomaly f_k if*

$$r(f_k) - R_{\male} \leq -100 \ km. \tag{16}$$

Crash events are considered when P_3 is below the planet surface. Subsurface solutions are computed for up to 100 km below P_2 radius. Therefore, it is easy to track the end of a WSB family to a physical collision.

Definition 4 (Classification). *Definitions 1−3 of revolution, escape, and crash are used to classify initial conditions that generate the trajectory $\boldsymbol{x}(f)$ (to which the definitions above are applied) when flown forward and backward under Eqs.* (6). *Orbits are classified into four mutually exclusive categories. The following sets of initial conditions are constructed according to the orbits they generate.*

- *Weakly stable set, $\mathcal{W}_{\pm n}$: contains initial conditions whose orbits perform n complete revolutions about P_2 before escaping [31].*
- *Escape set, $\mathcal{E}_{\pm}$: contains initial conditions whose orbits escape from P_2 without completing any revolution around it [31].*
- *Crash set, $\mathcal{K}_{\pm g}$: contains initial conditions whose orbits impact with P_2 after $g-1$ revolutions*

around it [31].

- *Persistent set, $\mathcal{P}_{\pm}$: contains initial conditions whose orbits do not escape from or impact with P_2 (likely performing several revolutions about it), within a specified maximum duration, $\Delta f_{\max}$.*

Plus and minus signs in the set names indicate forward and backward integration of the matching initial condition, respectively. Escape and Crash conditions are checked at every integration step. The integration is halted if either condition occurs. Completed revolutions around P_2 are checked a posteriori. Note that the indices definition of weakly stable and crash sets differs: index $\pm n$ of the weakly stable set indicates completion of n revolutions about P_2, while index $\pm g$ of the crash set refers to trajectories that crash before completing the g-th revolution about P_2.

In this work, Definition 2 of escape is Boolean, i. e., either an orbit escapes or it does not. In this framework, no other descriptors are added to specify affinity of initial conditions with the persistent set, $\mathcal{P}_{\pm}$. In view of this, a highly irregular trajectory would be classified as persistent, similarly to a trajectory that asymptotically approaches a single type of motion. This difference is accounted in Section V C, where the quality of ballistic captures is discussed.

A group of sample orbits about Mars is shown in Fig. 2. A few observations arise from the definitions above. (i) The definition of revolution solely relies on a geometrical criterion; i. e., P_3 completes a revolution about the smaller primary regardless of its Keplerian energy upon completion [16, 18, 36]. (ii) The persistent set, $\mathcal{P}_{\pm}$, is attached to the maximum duration of flight, $\Delta f_{\max}$. Namely, a given initial condition is persistent only within the simulation time. When longer $\Delta f_{\max}$ are considered,

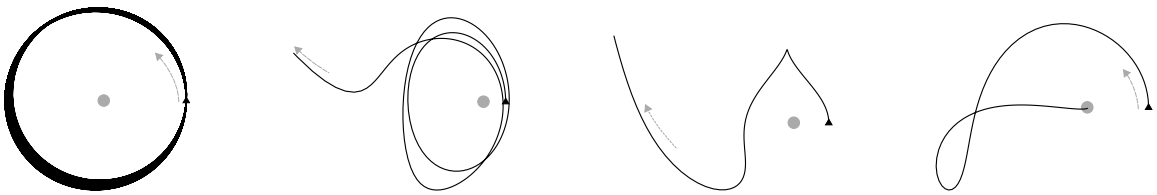

(a) Persistent, $\mathcal{P}_{+}$. (b) Weakly stable, $\mathcal{W}_2$. (c) Escape, $\mathcal{E}_{+}$. (d) Crash, $\mathcal{K}_1$.

Fig. 2: Orbits in the Sun–Mars ERTBP. The black triangle is the initial condition, the gray spot is Mars (not to scale). Arrows indicate direction of motion.

the ERTBP dynamics might cause the spacecraft to either collide or escape from P_2, leading to a different initial condition classification. In this paper, $\Delta f_{\max}$ is chosen corresponding to 100 years.

D. Construction of ballistic capture orbits

Two types of ballistic capture sets are identified by manipulating the persistent and weakly stable sets: the *finite capture set* $\mathcal{C}^n_{-m}$ and the *persistent capture set* $\mathcal{C}^\infty_{-m}$. These are found as intersection between sets that include orbits generated from propagation along opposite directions of independent variable. Thus, the intersection would result in a subset including only continuous orbits, compatibly with the theorem of existence and uniqueness of differential equations. The initial conditions in $\mathcal{C}^n_{-m}$ generate orbits that (1) perform m revolutions around P_2 before escaping from it when integrated backward, and (2) perform n revolutions in forward true anomaly without impacting or escaping [21];

$$\mathcal{C}^n_{-m} = \mathcal{W}_{-m} \cap \mathcal{W}_n. \tag{17}$$

On the other hand, initial conditions in $\mathcal{C}^\infty_{-m}$ generate orbits like $\mathcal{C}^n_{-m}$ except that the forward motion is persistent around P_2 for the whole flight duration;

$$\mathcal{C}^\infty_{-m} = \mathcal{W}_{-m} \cap \mathcal{P}_+. \tag{18}$$

The persistent capture set $\mathcal{C}^\infty_{-m}$ represents an addition and expands the concept of WSB to account for solutions that remain persistently trapped in the vicinity of Mars in a weakly captured state (in the timeframe of the simulation). From a mission analysis perspective, the most desirable situation is $\mathcal{E}_- \cap \mathcal{P}_+$. The orbits generated from these sets are indeed good candidates to design ballistic capture solutions upon arrival at a planet or moon. These solutions come from outside of P_2 SOI with positive Kepler energy, and perform ideally a large number of complete revolutions at a completely *zero-cost basis*, without escaping or impacting P_2 within the maximum set $\Delta f_{\max}$. In the formalism of the patched-conics method, the pre-capture occurs resembles a hyperbola (albeit

low-energy), whereas the post-capture shows a repetitive, quasi-regular behavior, typical of two-body motion. This dichotomy is achieved by exploiting the natural dynamics of the ERTBP: no orbital maneuvers are necessary. A detailed summary of the developed algorithm to construct the sets, manipulate them, and practically extract the ballistic capture solutions is outlined in Table 2.

Table 2: Algorithm to design practical ballistic capture solutions in the planar ERTBP.

1. **Initialization**
   Select primaries (e. g., Sun–Mars) and load their physical parameters (see Table 1)
2. **Periodic orbits computation** (For more details see Russell (2006) [40])
   Set the CRTBP as default dynamical model, Eqs. (1)
   Set bounds for search variables $x_0^{(c)} \in [x_{0_{\min}}^{(c)}, x_{0_{\max}}^{(c)}]$, $v_0^{(c)} \in [v_{0_{\min}}^{(c)}, v_{0_{\max}}^{(c)}]$ and discretize them
   Set number of revolutions, N_r, around P_2, and maximum period of the periodic orbits
   Perform differential correction on search grid
   Save periodic orbits solutions in $(x_0^{(c)}, v_0^{(c)})$ pairs and orbit period T
3. **Ballistic capture solution construction**
   Set the ERTBP as default dynamical model, Eqs. (6)
   Select (a) stability range, k_1, and (b) $x_0^{(c)}$ boundaries
   Load periodic solutions, $(x_0^{(c)}, v_0^{(c)})$, according to k_1 and $x_0^{(c)}$ boundaries in matrix $\Sigma \in \mathbb{R}^{N_s \times 2}$
   Set the number of initial true anomaly samples, n_f, and map parameter samples, n_k
   Set boundaries for map parameter k, $k \in [k_{\min}, k_{\max}]$
   Discretize the initial true anomaly f_0 by df_0, and the map parameter k by dk
   Set the maximum $\Delta f_{\max}$, and the maximum number of x axis crossings, N_x
   FOR $ii = 1$ to $ii = N_s$ by 1
      Extract current initial condition from $\Sigma \rightarrow \boldsymbol{x}_0^{(c)} = (x_0^{(c)}, 0, 0, v_0^{(c)})^{\mathrm{T}}$
      FOR $f_0 = 0$ to $f_0 = 2\pi$ by df_0
         FOR $k = k_{\min}$ to $k = k_{\max}$ by dk
            Apply mapping $\mathcal{F}(k) : \boldsymbol{x}_0^{(c)} \rightarrow \boldsymbol{x}_0$, Eq. (10), to get ERTBP initial condition, $\boldsymbol{x}_0$
            Integrate $(f_0, \boldsymbol{x}_0)$ until (15) or (16) are true or $f_0 \pm \Delta f_{\max}$ or N_x is reached
            Store forward and backward true anomalies, $f^{\pm}$, for which above conditions are met
            Classify initial conditions with to Definition 4, and generate sets $\mathcal{P}_{\pm}$, $\mathcal{W}_{\pm n}$, $\mathcal{E}_{\pm}$, $\mathcal{K}_{\pm g}$
         ENDFOR k
      ENDFOR f_0
   ENDFOR ii
   Extract capture sets $\mathcal{C}_{-m}^{n}$ and $\mathcal{C}_{-m}^{\infty}$ by intersecting initial conditions sets according to (17)-(18)
4. **Post-processing and analysis**
   Compute geometrical and physical properties of periodic orbits (J, stability, etc.)
   Reconstruct each ballistic capture solution within $f = [f^-, f^+]$ by backward/forward integration
   Compute and draw capture sets properties and trend (H_2, altitude profiles, number of revolutions, regularity, osculating parameters, approaching direction, TOF, etc.)
   Select desired ballistic capture trajectories according to mission requirements

E. Quality of the ballistic capture

The capture sets defined in Eqs. (17)-(18) are made of points that depend upon the search space variables (k, f_0) discretization. A fine discretization is generally favored not to lose possible interesting dynamics. However, many ballistic capture solutions may not be practical for application, since they correspond to chaotic high-sensitivity trajectories. The quality of the ballistic capture needs therefore to be evaluated. The ballistic capture trajectory is ideal when appears regular and repetitive, much like it would occur in a two-body ellipse. For these solutions, the particle approaches P_2 and describes N_r closed orbits around it having similar shape and orientation. A regular post-capture orbit possesses two advantages: (1) it allows multiple insertion options, and (2) it permits to better plan the post-capture phase and better analyze the mission requirements.

The quality of the capture solutions is measured by the *regularity index* [31], S,

$$S = \frac{f_{N_r} - f_0}{N_r}, \qquad S^{(2b)} = \frac{2\pi}{\sqrt{\mu}} \left(\frac{r_0}{1 - e_0} \right)^{3/2}, \qquad \Delta S_{\%} = 100 \left| \frac{S}{S^{(2b)}} - 1 \right|, \tag{19}$$

where N_r is the number of forward or backward revolutions completed by the particle, f_0 is the initial system true anomaly, f_{N_r} is the system true anomaly corresponding to completion of the N_r-th revolution of P_3 about P_2. In [31], S is called stability index. To avoid confusion with the periodic orbit stability index, k_1, the name has been adjusted to regularity index in this work. It has been shown that S embeds sufficient information to characterize the regularity of the ballistic capture [35]. $S^{(2b)}$ is the regularity index of a Keplerian orbit at the periapsis of an osculating ellipse with pericenter r_0 and eccentricity e_0. There is evidence that regular capture orbits feature values of the regularity index that are close to their Keplerian counterpart [32]. The distance between S and $S^{(2b)}$ is measured by the regularity coefficient, $\Delta S_{\%}$, and indicates how far an orbit is from being Keplerian. In this work, the regularity coefficient is used solely to characterize a geometrical qualitative feature of the ballistic capture, not a dynamical property. If the osculating conic is a parabola or a hyperbola, $\Delta S_{\%}$ is set to a negative value and is not representative of the actual regularity of the trajectory.

V. Results

In this Section, the Sun–Mars system is taken as case study for the application of the process described above. In particular, (1) families of simple periodic orbits about Mars are found in the Sun–Mars planar CRTBP; and (2) these orbits are mapped through $\mathcal{F}(k)$ in Eq. (10) to the Sun–Mars planar ERTBP for the construction of initial conditions and capture sets that lead to ballistic capture at Mars. The families of simple symmetric periodic orbits (1 revolution) that circulate P_2 catch the dominant features of the motion in the vicinity of P_2. Three simple planar periodic orbit families are sought in this class. Note that Lyapunov orbits around Lagrange points have been computed as a by-product, but are not utilized further.

A. Periodic orbits in the CRTBP

The differential corrector scheme [40] is applied to 10.5 million starting points. The algorithm in Table 2 is applied first with a course mesh with liberal values for ranges on the search space $(x_0^{(c)}, v_0^{(c)})$ to determine appropriate mesh sizes and ranges for later more refined searches. Table 3 presents the final uniform mesh parameters and bounds. In total, 2653 Mars-circulating simple symmetric periodic solutions have been sequentially found using roughly 9 hours on a 2.9 GHz Intel Core $i7$ Unix machine and a $7^{\text{th}}/8^{\text{th}}$ order variable step Runge–Kutta–Fehlberg scheme implemented within a Matlab mex file, and absolute and relative error tolerances 2.5×10^{-14}. Of the periodic families of interest, approximately 39% were classified as stable, 30% were found mildly unstable, and 31% unstable (see Section III). In view of the high computational cost to compute the periodic orbits, a grid search approach is preferred in this work, rather than a continuation technique, because the grid search method is more apt to extension to the spatial problem.

Table 3: Search regions for Sun–Mars periodic orbits.

Search region	$x_{0_{\min}}^{(c)}$	$x_{0_{\max}}^{(c)}$	$\#\ x_0$	$v_{0_{\min}}^{(c)}$ [km/s]	$v_{0_{\max}}^{(c)}$ [km/s]	$\#\ v_0$
Retrograde	x_{L_1}	surface	500	0	2.41	5000
Direct	surface	x_{L_2}	1500	0	2.41	12000

Figs. 3–4 represent a complete picture of the single-periodic planar solutions near Mars, and circulating about it. In Figs. 3a–3d, the synodic Mars-centered initial position along x, Jacobi constant, period, and osculating parameters of the periodic orbits are plotted. The variables are grouped according to their stability index (black stable, dark shading mildly unstable, and light shading unstable). Osculating semi-latus rectum, p_0, and eccentricity, e_0, are computed by applying two-body formulas [55] to the areocentered initial condition as transformed from the CRTBP. Osculating semi-latus rectum is used, rather than osculating semi-major axis, because p_0 is always well defined for varying osculating eccentricities, whereas osculating semi-major axis is a discontinuous indicator.

Fig. 3c displays the Jacobi constant and the Mars-centered x position: three distinct families are

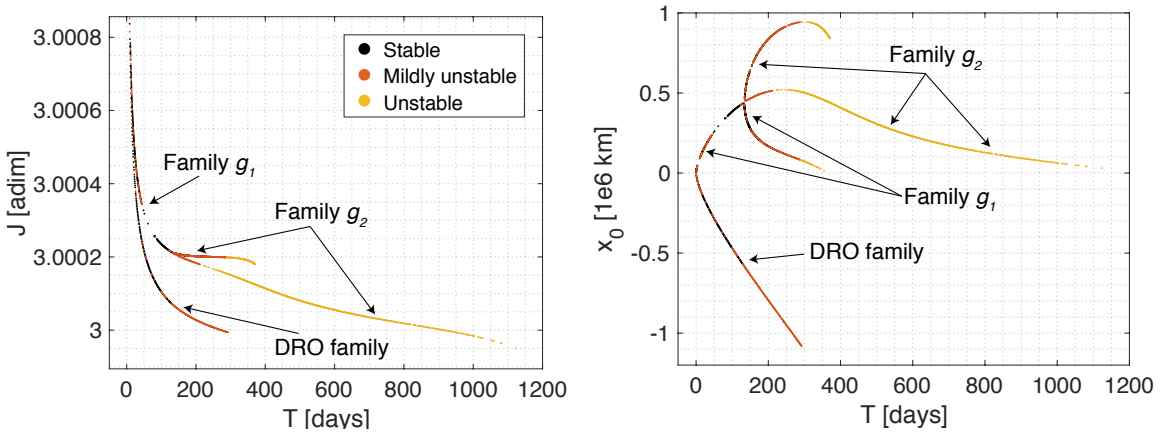

(a) Period vs Jacobi constant.

(b) Period vs Mars-centered x-coordinate.

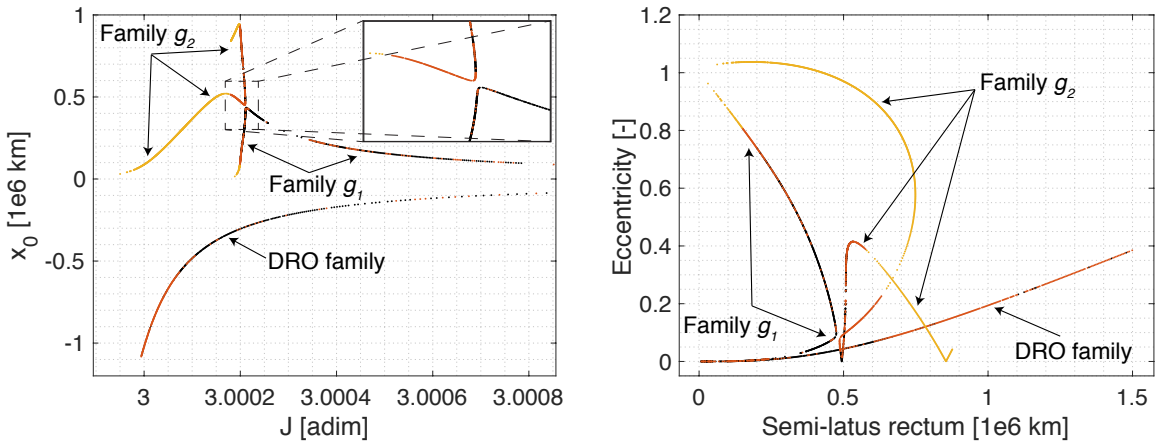

(c) Jacobi constant vs Mars-centered x-coordinate.

(d) Osculating semi-latus rectum vs eccentricity.

Fig. 3: POs scatter plots of relevant variables. Each point corresponds to a different trajectory.

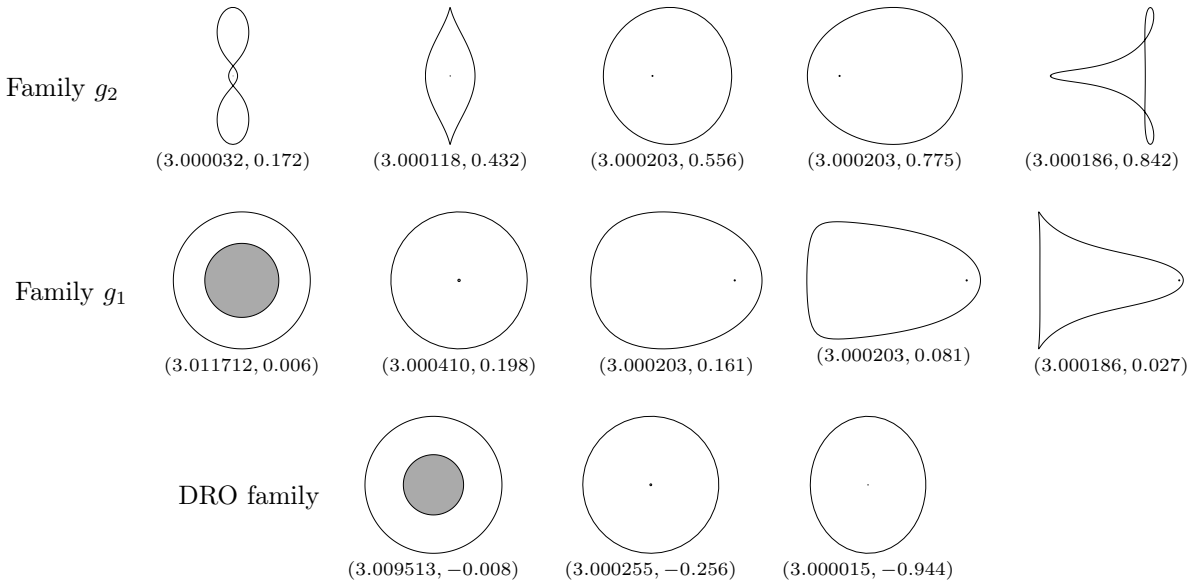

Fig. 4: Evolution of PO families. Coordinates are J [nondimensional units] and x_0 [10^6 km] on Fig. 3c. Grey spot represents Mars to scale.

recognized. The solutions are manually grouped as families and termed as Distant Retrograde Orbits (DRO), g_1 and g_2 [56]. These families are the same, albeit with different terminology, to those in [39, 40, 57]. The evolution of the families is outlined in Fig. 4 for different values of Jacobi constant. Henon's g and g' families in the Hill model intersect, whereas Fig. 3c (upper right zoom) shows a clear gap between the g_2 and g_1 families [58].

DRO solutions are never unstable. On the other hand, families g_2 and g_1 contain stable, mildly unstable, and unstable solutions. Unstable solutions of family g_1 mostly gather for low values of Jacobi constant, $J \leq 3.0002$. Conversely, a clear majority of family g_2 solutions exhibit (mildly) unstable behavior. For the observed orbit families at the constrained value of the mass ratio, periodic solutions tend to become more unstable as the period increases; this trend is clearly visible in Fig. 3a and Fig. 3b (light colored unstable dots are predominant in the right tail of the families, that is for higher values of T). On the other hand, no clear link is present between stability index and x_0.

Interestingly, the periodic families are well recognizable also when comparing osculating semi-latus rectum and eccentricity in Fig. 3d. In a two-body sense, osculating parabolas and hyperbolas exist within orbits of the g_2 family (see Fig. 3d). These are of particular interest for ballistic capture purposes as a higher approaching Keplerian energy generally yields a reduction of the

heliocentric duration to rendezvous with the planet [59]. A highly energetic approach that turns into a ballistic capture requires harnessing the dynamics of the pulsating system to slow down the particle and temporarily trap it about the planet [35]. As expected, all the larger-than-one osculating eccentricity orbits belong to the unstable g_2 family. Families g_2 and g_1 span the whole range of elliptical osculating eccentricity (also, osculating circular motion exists in two regions for family g_2), whereas the DRO family becomes monotonically more elliptic (with the apsides line directed as the synodic y axis) as their amplitude increases, with $e \approx 0.4$ at the libration points.

B. Ballistic capture at Mars in the ERTPB

The one-parameter dynamical map in Eq. (10) is applied to all the areocirculating periodic solutions, organized in $\{x_0^{(c)}, v_0^{(c)}\}_{j=1}^{N_s}$ pairs, $N_s = 2653$, for varying values of initial true anomaly. The true anomaly, $\{f_0^{(j)}\}_{j=1}^{n_f=120}$, is discretized in equally spaced 3° segments that span the whole orbital motion of Mars around the Sun. The map parameter is divided in $n_k = 399$ equally spaced samples. The resulting discrete vector, $\{k^{(j)}\}_{j=1}^{n_k}$, contains the unity value corresponding to the identity map, $\mathcal{F}(k) = \mathcal{I}$ when $k = 1$. With this discretization, over 127×10^6 initial conditions, $(f_0, \boldsymbol{x}_0)$, are forward and backward propagated in the ERTBP until conditions from Eqs. (15) or (16) are verified or either propagation limits $f_0 \pm \Delta f_{\max}$ or N_x are reached. For families $g_{1,2}$ $N_x = 50$, whereas $N_x = 500$ for DROs. According to Definition 4, these initial conditions are classified as persistent, weakly stable, escape, or crash sets; $\mathcal{P}_\pm$, $\mathcal{W}_{\pm n}$, $\mathcal{E}_\pm$, $\mathcal{K}_{\pm g}$, respectively. Finally, ballistic capture solutions are extracted by intersecting these sets as per conditions from Eqs. (17)-(18).

Surprisingly enough, 29.32% of the search space (i. e., 37.2×10^6 solutions) are found to be in one of the capture sets. For comparison, the WSB algorithmic definition implemented in Luo et al. [32] found that 0.0295% of the search grid space in the Sun–Mars ERTBP belonged to the $\mathcal{C}_{-1}^6$ capture set (refer to capture ratio in Table 3 therein). In the present study, 15.28% of the ballistic capture solutions perform at least 6 complete revolutions around Mars before escaping. The increase in captured solutions recovered by the present method is conjectured to be caused by the different grid search topology of the methods: (a) the exploitation of periodic motion to study ballistic captures

(this work) allows to sweep a wide variety of osculating conditions around Mars, ranging from ellipses to hyperbolas; on the other hand (b) the algorithmic definition applied in [32] is limited to very elliptical osculating conditions (i. e., $e_0 = 0.95$) that circulate in osculating argument of pericenter and at closer distances with respect, for instances, to initial conditions originating from DROs.

Six samples of ballistic capture solutions are shown in Figs. 5–6, corresponding to different combinations of generating POs family and stability. Table 4 shows key parameters to reconstruct these solutions. In the first column of Figs. 5–6 a topographic map is shown representing the total number of forward (N_r^+) plus backward (N_r^-) revolutions around Mars as function of the search space (k, f_0), counted according to Definition 1. Each topographic map refers to one generating periodic orbit. In all 2653 cases, the map is symmetric with respect to the $f = \pi$ axis. Since the ERTBP equations of motion are even in f (due to the cosine term in the pseudo-potential, ω), this symmetric outcome was expected, and can be used to halve the search space. Each point in this map univocally specifies the initial conditions (x_0, v_0, f_0) for a potential ballistic capture solution. There is a wide variation in the number of weakly stable revolutions both across families and stability parameter. In Figs 5a and 5j the existence of capture sets seems to be confined within well-defined boundaries. The gradient of the revolutions number along k is very pronounced within these boundaries. This trend provides predictable regions in which ballistic capture solutions are likely to be found. On the other hand, weakly captured initial conditions are more numerous for the mildly unstable and unstable periodic solutions in the g_2 family (Figs. 5d and 5g). These initial conditions are preferred if quantity of the solutions is the driving factor. As expected, there are regions of the search space in which ballistic capture does not exist. Fig. 6d shows extremely limited options for P_3 to achieve a weakly captured state. However, these extremely rare events, localized at $k \cong k_{\min}$ and $f_0 \cong 350°$, generate solutions of interest for application as they are part of the persistent capture set. Since the generating orbits exist also in the CRTBP at the mass ratio of the Earth–Moon system [60], these types of solutions could be of interest, for instance, for NASA's Asteroid Redirect Mission (ARM) at the Moon [61].

The second and third columns of Figs. 5–6 display the behavior of one particular point in the

topographic map (light dots highlighted in each map corresponding to specified values of k and f_0). In particular, Figs 5b, 5e, 5h, 5k, 6b, and 6e show the backward (E^-, dark line) and forward (E^+, light line) motion of solutions within the capture sets. Generating periodic orbits (C, dashed dark closed line) and CRTBP zero-velocity curves (dashed light line) are also shown for reference. The trajectories of Figs 5b and 5e display regular motion around Mars, before escaping through $L_{1,2}$. Although the other sample trajectories exhibit a more irregular motion, they get closer to Mars than the regular orbits. This feature is observed in the vast majority of the solutions, and there seems to exist a trade-off between regularity of the solution and repeated P_2 close passages. The trajectory of Fig. 6e belongs to the $\mathcal{C}^{\infty}_{-m}$ set. Coming from the Sun side, P_3 is weakly captured at Mars and performs 310 revolutions about it without escaping for approximately 91.9 years. This capture is achieved on a zero-cost basis. The particle will eventually escape, simply employing a longer $\Delta f_{\max}$ than is used for the present simulations. P_3 gets closer than 10^5 km to Mars 125 times (averagely 4 times every 3 years), providing a discrete number of opportunities to permanently trap the orbit around Mars (via propulsion).

In the third column of Figs. 5–6, altitude and Kepler energy profiles of the same orbit are shown. These plots exhibit a repetitive signature: (a) the particle reaches Mars with a positive Kepler energy, (b) in the weakly captured phase H_2 fluctuates around a negative value, and then (c) P_3 escapes retracing again an osculating hyperbola. Note how Definition 2 of escape is well posed. Being geometrically situated outside the SOI is not a sufficient condition to guarantee that the particle will cease revolving around Mars.

The quality and regularity of ballistic capture solutions are yet other important factors when applicability to mission scenarios is considered. Fig. 7 shows the regularity coefficient, $\Delta S_{\%}$ from

Table 4: Initial conditions and key parameters of ballistic captures shown in Figs. 5–6.

	$x_0^{(c)}$ [adim.]	$v_0^{(c)}$ [adim.]	k [-]	f_0 [deg]	f^- [deg]	f^+ [deg]
Fig. 5a	1.001085292502152	0.023147929623056	1.184093091652790	300	−70.72963	437.37801
Fig. 5d	1.054270217770476	1.002232035596414	0.010928959027259	6	−402.03486	400.61490
Fig. 5g	1.002941622483471	0.006170022665865	0.995792311239681	258	−1500.27638	791.36927
Fig. 5k	1.000765344843256	0.025326253817461	0.995792311239681	93	−19.12681	782.20914
Fig. 6a	0.995431558509543	0.014322449245684	0.991584622479361	147	−1593.52443	1239.83258
Fig. 6d	0.999121563467277	0.020085493679947	0.832533987339290	339	−3322.99062	14267.36542

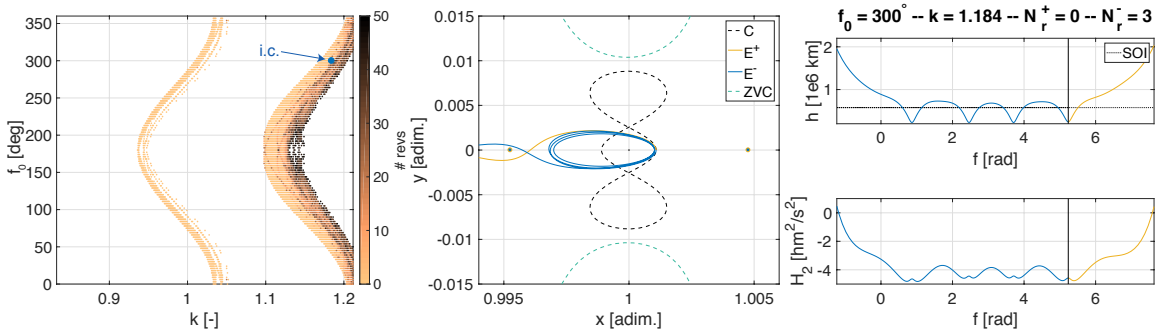

(a) g_2-family unstable solutions. (b) Weak capture trajectory sample. (c) Altitude (top), energy (bottom).

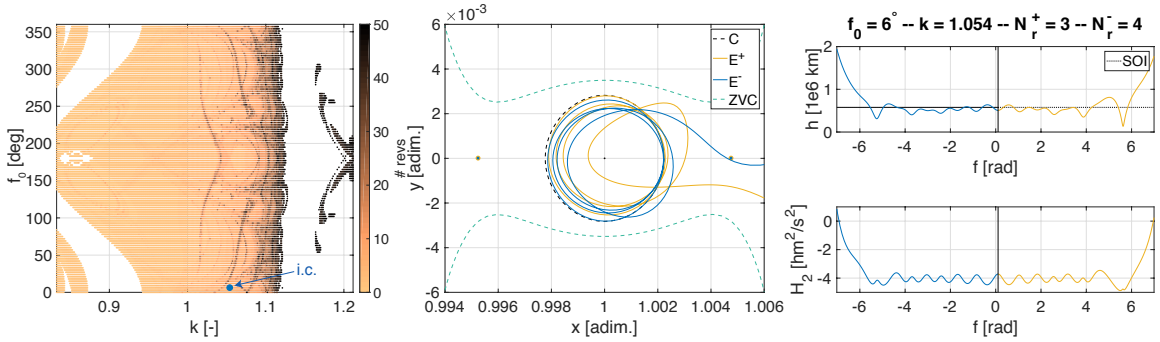

(d) g_2-family mildly unstable solutions. (e) Weak capture trajectory sample. (f) Altitude (top), energy (bottom).

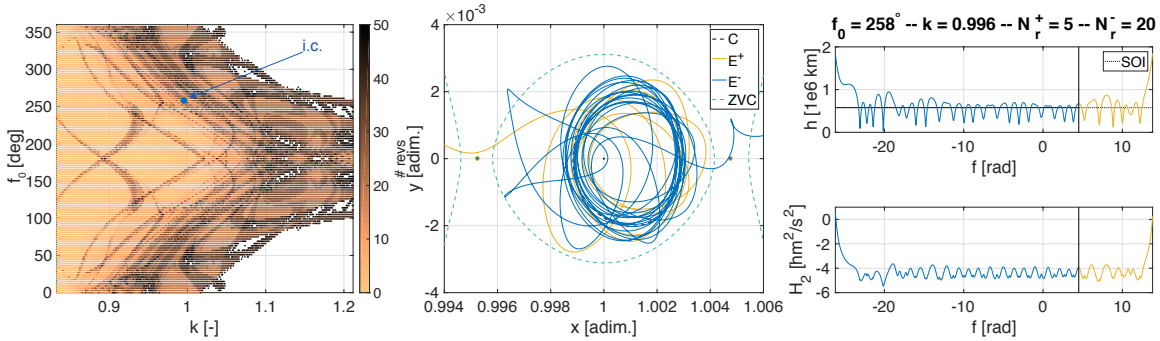

(g) g_2-family stable solutions. (h) Weak capture trajectory sample. (i) Altitude (top), energy (bottom).

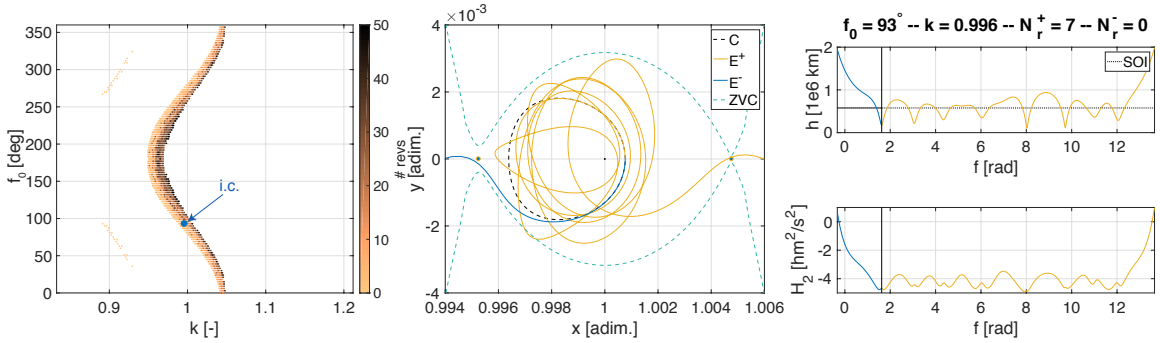

(j) g_1-family stable solutions. (k) Weak capture trajectory sample. (l) Altitude (top), energy (bottom).

Fig. 5: Samples of ballistic captures generating from families $g_{1,2}$. Kepler energy is in 10^4 m^2/s^2.

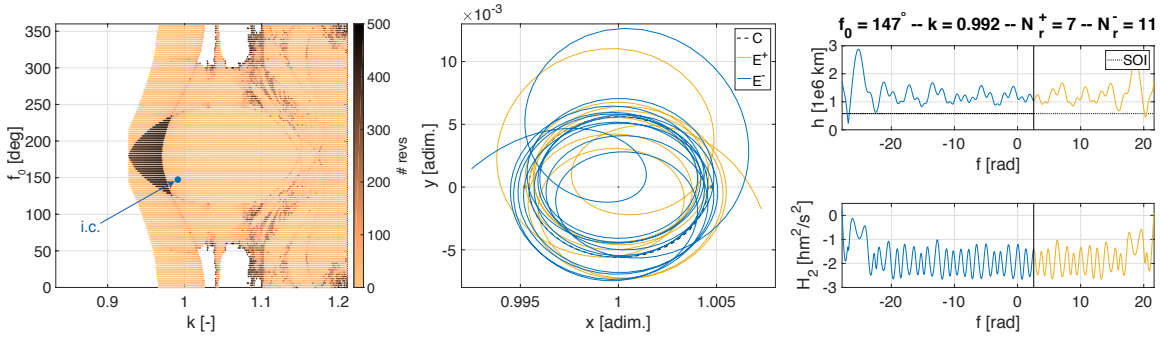

(a) DRO mildly unstable solutions. (b) Weak capture trajectory sample. (c) Altitude (top), energy (bottom).

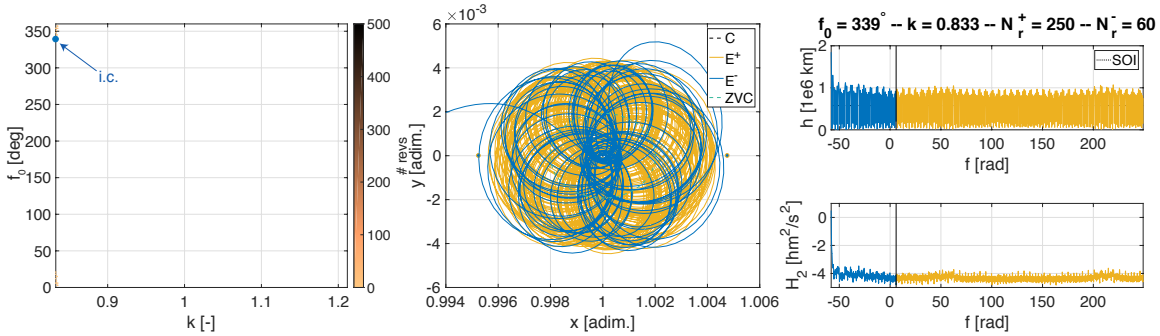

(d) DRO stable solutions. (e) Weak capture trajectory sample. (f) Altitude (top), energy (bottom).

Fig. 6: Samples of ballistic captures generating from DROs. Kepler energy is in 10^4 m^2/s^2.

Eq. (19), of three sets of ballistic capture solutions (only the forward part of the set is shown here). The particularly evident empty island in Fig. 7a, formed around $f_0 \cong 220°$ and $k \cong 0.88$, has its symmetric counterpart when the regularity coefficient is studied for the backward subset. In this region, hyperbolic and parabolic osculating initial conditions give rise to motion that cannot be compared with a two-body trajectory, in terms of the regularity index. The points belonging to

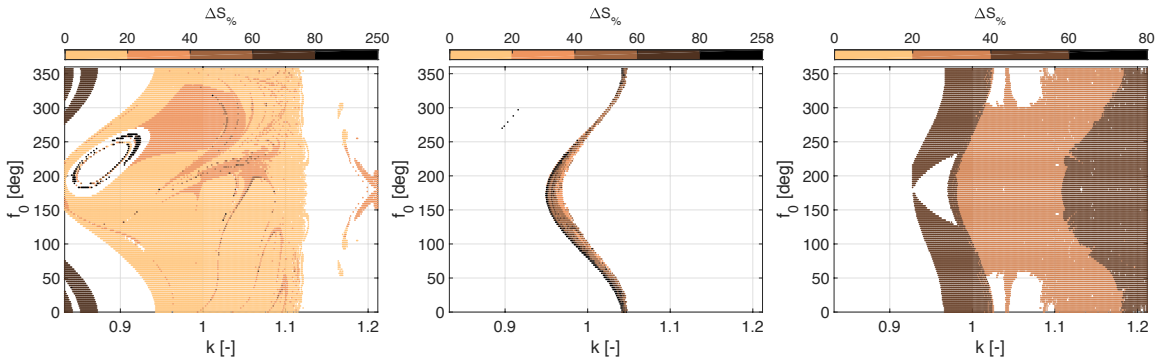

(a) Family g_2 mildly unstable solutions (affinity with Fig. 5d). (b) Family g_1 stable solutions (affinity with Fig. 5j). (c) DRO family mildly unstable solutions (affinity with Fig. 6a).

Fig. 7: The regularity coefficient, $\Delta S_{\%}$, for the sole forward part of the sets.

the island boundaries are very far from being Keplerian, with $\Delta S_{\%} > 80$. In this case, regular solutions in forward integrations seem to gather for $f_0 \in [0, 180]$ degrees, i. e., when Mars is near perihelion and flying away from the Sun with positive radial velocity. The family g_1 stable case (refer to Fig. 7b) solutions become more regular as the map parameter is increasing within the bounded region. Thus, a more persistent solution is also likely to exhibit a more regular motion. Lastly, ballistic solutions that generate from DROs generally have very persistent, mildly irregular behavior, with $\Delta S_{\%} \in [40, 80]$. The empty island in the middle left part in Fig. 7c is associated with extremely persistent motion (i. e., the persistent capture set $\mathcal{C}^{\infty}_{-m}$).

C. Global characterization of ballistic capture solutions

A global portrait essentially provides a comprehensive insight on how the ballistic capture mechanisms work. Nevertheless, a global characterization is difficult to obtain, because of both the dimensionality of the search space and the number of parameters that influence the survey (e. g., osculating parameters, stability of the generating initial conditions, primaries geometric configuration, grid discretization, etc.). In this study, the global portrait of the ballistic capture process is deemed to be well represented by four separated factors:

1. The capture ratio, $N_s^{\mathcal{C}}$, i. e., the percentile number of weakly captured solutions with respect to the search grid dimension, $n_f n_k$. For each generating periodic initial condition, the capture ratio is a measure of the occurrence of capture orbits in the total set of initial conditions. Through Fig. 3c the Jacobi constant is easily related to the position, and hence to the vertical velocity. These can be used to compute osculating pericenter radius and eccentricity.

2. The percentile number of weakly captured solutions which feature a regularity coefficient, $\Delta S_{\%}$, below a certain threshold. This figure is referred to $\Delta S^{\iota}_{\%}$, where ι is the percentile threshold. The scaling is here the number of solutions belonging to the capture sets for a fix generating initial condition, and not the grid dimension. This scaling better emphasizes the real trend of regularity within solution sets.

3. The number of backward and forward revolutions around P_2, termed N_r^- and N_r^+, respectively.

This is a direct indicator of the time P_3 dwells in the vicinity of the smaller primary in a weakly captured state.

4. The regularity of the solutions, expressed by the regularity coefficient, $\Delta S_{\%}$. Quasi-regular motion is generally a desired feature for trajectories in an applied context, and low values of $\Delta S_{\%}$ are preferred over chaotic difficult-to-predict trajectories.

While $N_s^{\mathcal{C}}$, $\Delta S_{\%}^{\iota}$, and N_r are quantitative indices, $\Delta S_{\%}$ is a qualitative measure of regularity for capture solutions only (see Section IV E). Indices N_r and $\Delta S_{\%}$ are shown as function of the initial osculating eccentricity and periapsis distance, e_0 and r_0, respectively. This choice is motivated to ease comparison with existing sets of ballistic captures.

Fig. 8a shows the capture ratio trend discriminating for family and stability index of the generating periodic orbit. The shading scheme is the same as that of Fig. 3. As J increases, the capture ratio of DROs (triangular markers) diminishes, until no ballistic capture practically occurs for $J \geq 3.000341$. Accordingly, DROs that originate closer to Mars (i. e., larger Jacobi constant) are less likely to generate weakly captured motion. The $N_s^{\mathcal{C}}$ trend for solutions of family g_1 (cross markers) remarkably retraces the $(J, x_0^{(c)})$ trend of the CRTBP simple periodic orbits. Unstable g_1 family motion is associated with very low values of capture ratio, no more than 1.7% were found to generate ballistic captures. On the other hand, stable and mildly unstable initial conditions show a

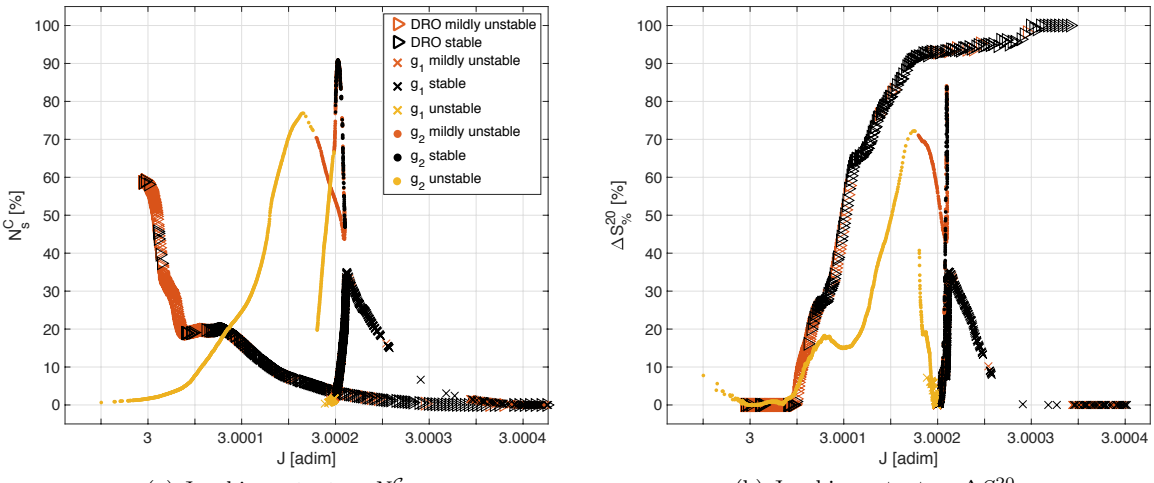

(a) Jacobi constant vs $N_s^{\mathcal{C}}$.

(b) Jacobi constant vs $\Delta S_{\%}^{20}$.

Fig. 8: Global quantitative trend of ballistic captures for varying energy of the generating POs.

peak at $N_s^{\mathcal{C}} \approx 35\%$. Capture ratio trend for family g_2 periodic orbits (dotted markers) is somewhat more complicated, due to the more complicated structure of this family (see orbit evolution diversity in Fig. 4). For the unstable part of the family, the number of ballistic captures increases with J. Stable and mildly unstable g_2 generators feature a faster variation across J, with a maximum of $N_s^{\mathcal{C}} \approx 90\%$. Considering the large number of solutions, DROs seem to be less effective generators of ballistic captures when compared to the $g_{1,2}$ families.

In Fig. 8b $\Delta S_{\%}^{20}$ is shown. The threshold of $\Delta S_{\%} \leq 20$ is chosen to represent a near-Keplerian capture condition. This value serves as an appropriate cut-off to discriminate between a geometric quasi-regular and irregular motion around Mars. The regularity trend of the DROs solutions is in contrasts with the abundance of the ballistic captures generating from them. Indeed, as the DRO starts closer to Mars (and hence generates fewer ballistic captures) there are more regular ballistic capture trajectories. The Pareto trade-off between regularity and abundance occurs across $J = 3.000064$ nondimensional units. Index $\Delta S_{\%}^{20}$ of families $g_{1,2}$ generally displays a concurrent trend with the capture ratio, except for the low J parts of the unstable groups.

Referring to Fig. 9, the totality of ballistic capture solutions is binned according to initial osculating eccentricity, e_0, and regularity coefficient of the sole forward phase, $\Delta S_{\%}$. The number of solutions in each bin, expressed as percentile of the total solutions, is hence represented as a two-dimensional gradient map. In this map, bins are considered empty if they contain less or equal than 0.01% of the available data. The shading is darker for bins with fewer solutions, and lighter for a larger

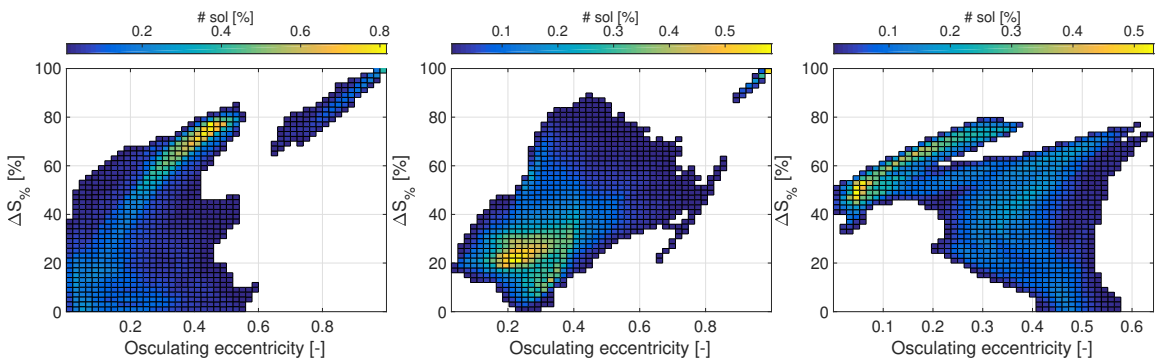

(a) Family g_2. (b) Family g_1. (c) DRO family.

Fig. 9: Gradient maps for regularity index and osculating eccentricity for binned solutions.

number of ballistic captures. A densely-populated island appears in the lower left part of Fig. 9b for ballistic capture generated from POs of family g_1. This region provides interesting opportunities to achieve quasi-regular motion around P_2 departing from small eccentricity osculating conditions. In Fig. 9a ballistic captures generating from g_2 periodic motion exist, albeit not numerous, for low osculating eccentricities and low regularity index. This area shrinks and becomes more densely populated as both e_0 and $\Delta S_{\%}$ increases. Ballistic captures of practical interest originating from DROs (Fig. 9c), with $\Delta S_{\%} \leq 20$, occurs at initial osculating eccentricities around $e_0 \approx 0.5$; yet most of the solutions feature nonregular post-capture behavior. Interestingly, ballistic captures originating from low osculating eccentricities and performing many revolutions around Mars are, in fact, quite common cases.

The persistence of the solutions as a global quantity is represented in Fig. 10. A longer ballistic capture trajectory generally provides multiple close passages; thus, potential opportunities to perform scientific observations or experiments at P_2 or to permanently close the system natural escape routes. In particular, the number of backward and forward revolutions that P_3 perform around Mars in a weakly captured state is shown as function of the initial osculating eccentricity, e_0, and osculating periapsis distance, r_0. It is important to note that initial osculating states might not be good indicators of how close and how frequently a specific ballistic capture trajectory passes in the

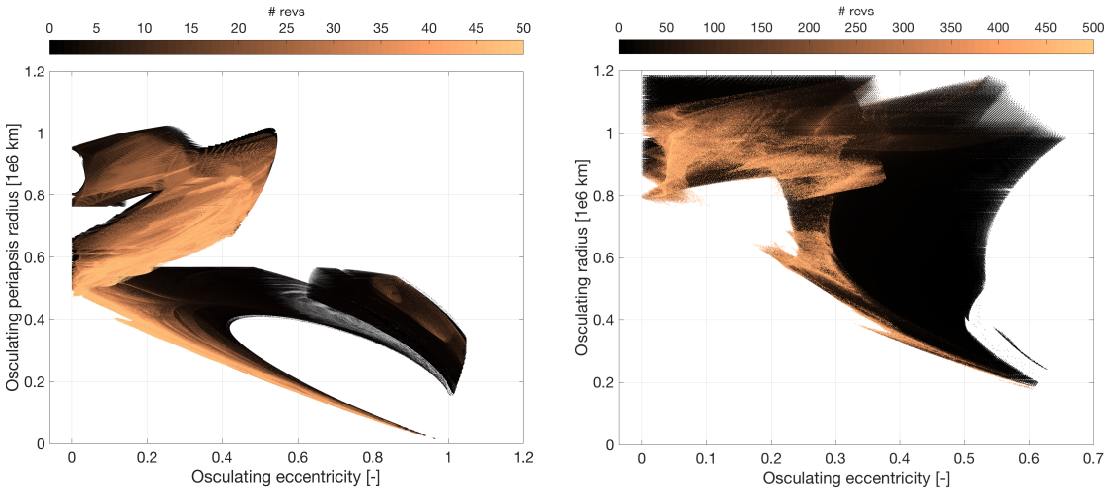

(a) Families g_2 and g_1.

(b) Family DRO.

Fig. 10: Number of ballistically captured forward/backward revolutions around P_2.

vicinity of P_2 for the whole flight duration. Each dot in the maps corresponds to a different ballistic capture solution. Approximately 32.8 and 4.4 million solutions are plotted in Fig. 10a and Fig. 10b, respectively. Solutions with a higher number of revolutions are marked with lighter colored dots. Ballistic captures originating from low osculating eccentricities and performing many revolutions around Mars represent an ordinary phenomenon. The majority of solutions originating at the periapsis of osculating hyperbolas perform at most a few revolutions before escaping, shadowing the difficulty to turn a highly energetic inbound trajectory to a weakly stable one. Ballistic captures that originate close to P_2 need to depart from a high elliptical osculating state to achieve weakly captured motion. Generally, as the initial osculating radius decreases, the existence region of ballistic captures shrinks, with a clear persistency signature for lower values of e_0 (i. e., spike-shaped structure in the bottom-right part of Fig. 10a). DROs offer a wider range of opportunity for ballistic solutions very far away from P_2.

D. Behavior in an ephemeris model

Capture orbits whose initial conditions are reported in Table 4, are now demonstrated to exist within a higher fidelity model. The behavior in an ephemeris model is helpful to show that ballistic captures may ultimately be used in a real mission scenario, albeit the main results and contributions of this work are found in the ERTBP. The ERTBP has fewer dimensions and more dynamical structure (i. e., insight to be gained) than the full ephemeris model. In this Section, the SPICE ephemerides of the Sun, Earth, Mars, Jupiter, and Saturn are used to better represent the dynamics. The integration is performed in the roto-pulsating restricted n-body problem (RPRnBP), a high-fidelity synodic model that has been thoroughly tested and validated [62, 63]. In the RPRnBP, the equations of motion for a massless particle in the solar system barycentric model are transformed such that the new frame of reference rotates and pulsates in a nonuniform fashion. The primaries are always aligned with the x axis of the new frame, and their positions are fixed in time with respect to the new frame of reference. This guarantees some convenient features, primarily suggested by the CRTBP. The RPRnBP is preferred to an areocentric inertial frame because it naturally retains the dynamical characteristics of the ERTBP.

It is shown here how weak capture solutions in the planar ERTBP can be extended to a spatial quasi-real solar system environment. The employed procedure is a simple one:

1. Retrieve the initial conditions defined in the planar ERTBP, and map them to the spatial RPRnBP. Transition from the ERTBP to the solar system model is achieved with the unity map, $\mathcal{F}(1)$, and setting to zero initial out-of-plane position and velocity components of the state in the RPRnBP.

2. Find the epoch that corresponds to the Sun–Mars initial true anomaly, f_0. This epoch is searched within January 1 2017 and November 20 2018, roughly embracing one Mars year.

3. Build an epochs grid across the date found in Step 2. The grid spans ± 15 days from the initial epoch, roughly corresponding to an angular offset of ± 10 degrees along Mars orbit, which is tested to be sufficient to extend ballistic capture from the ERTBP to the RPRnBP.

4. For every epoch in the grid, backward and forward propagate each initial condition in the RPRnBP and classify weak captures according to Definition 4.

Note that this analysis is not intended as a solution continuation per se, rather it aims at stressing the role simplified models play in the search for ballistic captures. Fig. 11 displays two samples of weak captures in the RPRnBP, Fig. 11a corresponding to the trajectory shown in Fig. 5k, and Fig. 11b to that of Fig. 5h. The weak capture generated from the g_1-family stable solution (refer to Fig. 11a) remarkably sticks close to its periodic CRTBP generator before escaping, both backward and forward in time, through a L_1 aperture. This solution departs 14 days before the epoch corresponding to f_0. On the other hand, the ballistic capture stemming from the g_2-family (refer to Fig. 11b) originates exactly when Mars is at f_0. In this case, the weak capture mechanism is similar to the ERTBP counterpart: the particle approaches Mars from the exterior (i. e., L_2) and escapes after few complete revolutions towards the interior (i. e., L_1).

In summary, (1) The out-of-plane motion of weak captures in the ephemeris-driven RPRnBP has a negligible component; (2) Solutions born in the ERTBP may be feasibly found to exist in a more realistic dynamical model, albeit with a qualitatively dissimilar motion, employing the initial epoch

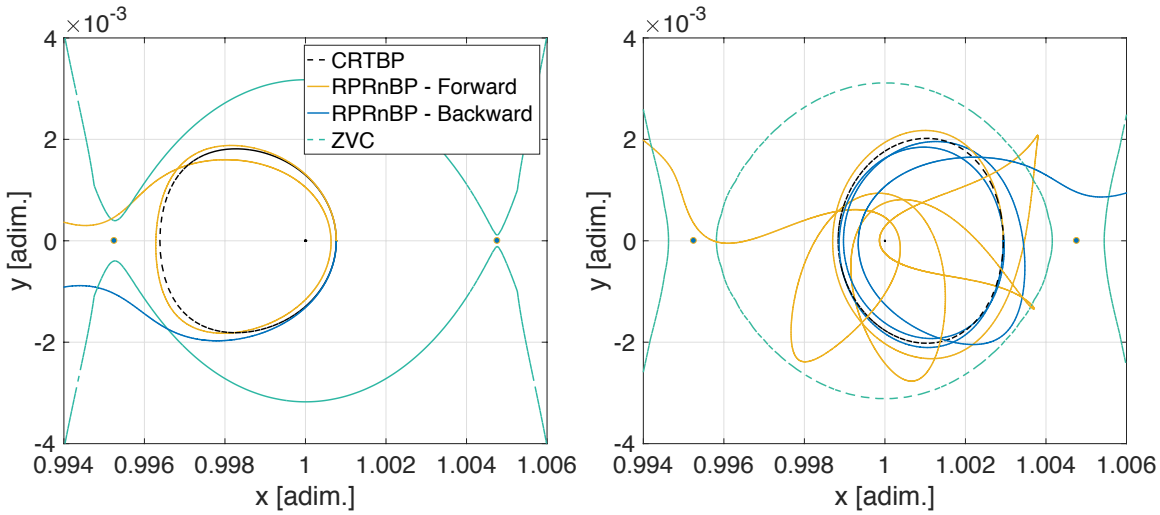

(a) g_1-family stable solution. Departure date: March 5 2018 18:08:22.1 Barycentric Dynamical Time (TDB).

(b) g_2-family stable solution. Departure date: April 10 2017 22:53:37.2 TDB.

Fig. 11: Samples of ballistic capture in the high-fidelity roto-pulsating frame (xy projection).

as the sole degree of freedom; and (3) The dynamics in the RPRnBP still retains, qualitatively, the stability properties of its generating orbits. While escape does eventually occur, it does not occur after the same number of revolutions or necessarily through the same gateway (L_1 versus L_2). Across the defined grid, none of the DROs produced a weak capture solution in the RPRnBP (trajectories remained stably confined in the vicinity of Mars), and most of the unstable $g_{1,2}$-family solutions resulted in fast-escaping trajectories. Conversely, solutions emanating from stable $g_{1,2}$ regions display a weak capture behavior also in the RPRnBP. As final remark, (4) Trajectories in the ERTBP and the RPRnBP do not track one another exactly, which is not surprising considering the associated chaotic sensitivities. However, similar stability and quality is demonstrated.

VI. Conclusions

In this work, a novel methodology is proposed to compute ballistic capture trajectories in the planar elliptic three-body problem for small eccentricities. Periodic motion of the planar restricted circular problem is used as a generator to trigger ballistic capture mechanisms in the Sun–Mars case, where the capture ratio improves by two orders of magnitude when compared to existing works. This approach is a paradigm shift: states are mapped from the circular to the elliptic problem with a single-parameter transformation and the initial true anomaly of the P_1P_2 system is parameterized.

By restricting the search to motion that emanates from the newly mapped initial conditions, the search space has been reduced by a full dimension (from four- to three-dimensional). A large scale survey is completed using 3 families of POs encompassing $2,653$ periodic solutions, which generated 37.2 million (29.32% of the search space) ballistic captures that are evaluated and classified for potential use. This methodology has shown that ballistic captures originating from low osculating eccentricities and performing many revolutions around P_2 exist in abundance. One example of a persistent trajectory is shown where P_3 stays in the vicinity of Mars, in a weakly captured state, for more than 90 years. Ultimately, ballistic captures in a high-fidelity dynamical model are computed starting from solutions within the planar ERTBP. The presented examples demonstrate feasibility in the continuation process of weak capture solutions towards a more realistic solar system environment.

A global analysis of the weakly captured solutions has shown a remarkable signature in the search space domain. As expected, periodicity is a persistent property that can be exploited to favor the generation of ballistic captures. Analysis on the post-capture qualitative behavior prunes many of the initial conditions in the capture sets due to the highly irregular motion around P_2. If quasi-regular motion is sought, close-to-P_2 DROs or far POs emanating from families g_1 and g_2 are good candidates. If the aim is to maximize P_3 persistence about Mars, sacrificing somewhat the regularity of the trajectory, large DROs are the best options, providing for hundreds of weakly stable revolutions. Asteroid capture missions, for instance, might profit from this mechanism to freely achieve long-term weakly stable motion. If the objective is to maximize robustness in achieving ballistic capture, family g_2 unstable POs around $J = 3.000164$ and stable POs around $J = 3.000202$ feature exceptionally high capture ratios.

Acknowledgments

This work was carried out at the University of Texas at Austin under a scholarship by the Italian Education, University, and Research ministry (MIUR).

References

[1] Belbruno, E. and Miller, J. K., "Sun-perturbed Earth-to-Moon transfers with ballistic capture," *Journal of Guidance, Control, and Dynamics*, Vol. 16, No. 4, 1993, pp. 770–775, doi:10.2514/3.21079.

[2] Jehn, R., Campagnola, S., Garcia, D., and Kemble, S., "Low-thrust approach and gravitational capture at Mercury," in "18th International Symposium on Space Flight Dynamics," Vol. 548, 2004, pp. 487–492.

[3] Belbruno, E. and Carrico, J. P., "Calculation of weak stability boundary ballistic lunar transfer trajectories," *AIAA/AAS Astrodynamics Specialist Conference*, Vol. 4142, 2000, pp. 262–271, doi:10.2514/6.2000-4142.

[4] Topputo, F. and Belbruno, E., "Earth–Mars transfers with ballistic capture," *Celestial Mechanics and Dynamical Astronomy*, Vol. 121, No. 4, 2015, pp. 329–346, doi:10.1007/s10569-015-9605-8.

[5] Circi, C. and Teofilatto, P., "On the Dynamics of Weak Stability Boundary Lunar Transfers," *Celestial Mechanics and Dynamical Astronomy*, Vol. 79, No. 1, 2001, pp. 41–72, doi:10.1023/A:1011153610564.

[6] Ivashkin, V. V., "On trajectories of Earth–Moon flight of a particle with its temporary capture by the Moon," *Doklady Physics*, Vol. 47, No. 11, 2002, pp. 825–827, doi:10.1134/1.1526433.

[7] Belbruno, E. and Miller, J., "A ballistic lunar capture trajectory for the Japanese spacecraft Hiten," *Jet Propulsion Laboratory, IOM*, Vol. 312, 1990, pp. 90–94.

[8] Racca, G. D., Marini, A., Stagnaro, L., van Dooren, J., di Napoli, L., Foing, B. H., Lumb, R., Volp, J., Brinkmann, J., Grünagel, R., Estublier, D., Tremolizzo, E., McKay, M., Camino, O., Schoemaekers, J., Hechler, M., Khan, M., Rathsman, P., Andersson, G., Anflo, K., Berge, S., Bodin, P., Edfors, A., Hussain, A., Kugelberg, J., Larsson, N., Ljung, B., Meijer, L., Mörtsell, A., Nordebäck, T., Persson, S., and Sjöberg, F., "SMART-1 mission description and development status," *Planetary and Space Science*, Vol. 50, No. 14–15, 2002, pp. 1323–1337, doi:10.1016/S0032-0633(02)00123-X.

[9] Chung, M. J., Hatch, S. J., Kangas, J. A., Long, S. M., Roncoli, R. B., and Sweetser, T. H., "Trans-lunar cruise trajectory design of GRAIL (gravity recovery and interior laboratory) mission," *AIAA/AAS Astrodynamics Specialist Conference*, Vol. 8384, 2010, pp. 1–16, doi:10.2514/6.2010-8384.

[10] Elliott, J. and Alkalai, L., "Lunette: A network of lunar landers for in-situ geophysical science," *Acta*

Astronautica, Vol. 68, No. 7–8, 2011, pp. 1201–1207,
doi:10.1016/j.actaastro.2010.10.024.

[11] Vetrisano, M., Van der Weg, W., and Vasile, M., "Navigating to the Moon along low-energy transfers," *Celestial Mechanics and Dynamical Astronomy*, Vol. 114, No. 1, 2012, pp. 25–53,
doi:10.1007/s10569-012-9436-9.

[12] Urrutxua, H., Scheeres, D. J., Bombardelli, C., Gonzalo, J. L., and Pelaez, J., "Temporarily captured asteroids as a pathway to affordable asteroid retrieval missions," *Journal of Guidance, Control, and Dynamics*, Vol. 38, No. 11, 2015, pp. 2132–2145,
doi:10.2514/1.G000885.

[13] Belbruno, E., "Lunar capture orbits, a method of constructing earth moon trajectories and the lunar gas mission," in "19th International Electric Propulsion Conference, Colorado Springs, CO," Vol. 1, 1987, p. 1054.

[14] Belbruno, E., "Ballistic lunar capture transfers using the fuzzy boundary and solar perturbations: a survey," *Journal of the British Interplanetary Society*, Vol. 47, No. 2, 1994, pp. 73–80.

[15] Belbruno, E., *Capture dynamics and chaotic motions in celestial mechanics: With applications to the construction of low energy transfers*, Princeton University Press, 2004.

[16] García, F. and Gómez, G., "A note on weak stability boundaries," *Celestial Mechanics and Dynamical Astronomy*, Vol. 97, No. 2, 2007, pp. 87–100,
doi:10.1007/s10569-006-9053-6.

[17] Sousa Silva, P. A. and Terra, M. O., "Applicability and dynamical characterization of the associated sets of the algorithmic weak stability boundary in the lunar sphere of influence," *Celestial Mechanics and Dynamical Astronomy*, Vol. 113, No. 2, 2012, pp. 141–168,
doi:10.1007/s10569-012-9409-z.

[18] Topputo, F. and Belbruno, E., "Computation of weak stability boundaries: Sun–Jupiter system," *Celestial Mechanics and Dynamical Astronomy*, Vol. 105, No. 1, 2009, p. 3,
doi:10.1007/s10569-009-9222-5.

[19] Topputo, F., Belbruno, E., and Gidea, M., "Resonant motion, ballistic escape, and their applications in astrodynamics," *Advances in Space Research*, Vol. 42, No. 8, 2008, pp. 1318–1329,
doi:10.1016/j.asr.2008.01.017.

[20] Belbruno, E., Topputo, F., and Gidea, M., "Resonance transitions associated to weak capture in the restricted three-body problem," *Advances in Space Research*, Vol. 42, No. 8, 2008, pp. 1330–1351,
doi:10.1016/j.asr.2008.01.018.

[21] Hyeraci, N. and Topputo, F., "Method to design ballistic capture in the elliptic restricted three-body problem," *Journal of guidance, control, and dynamics*, Vol. 33, No. 6, 2010, pp. 1814–1823, doi:10.2514/1.49263.

[22] Paskowitz, M. E. and Scheeres, D. J., "Robust capture and transfer trajectories for planetary satellite orbiters," *Journal of guidance, control, and dynamics*, Vol. 29, No. 2, 2006, pp. 342–353, doi:10.2514/1.13761.

[23] Sousa Silva, P. A. and Terra, M. O., "Diversity and validity of stable-unstable transitions in the algorithmic weak stability boundary," *Celestial Mechanics and Dynamical Astronomy*, Vol. 113, No. 4, 2012, pp. 453–478, doi:10.1007/s10569-012-9418-y.

[24] Romagnoli, D. and Circi, C., "Earth–Moon Weak Stability Boundaries in the restricted three and four body problem," *Celestial Mechanics and Dynamical Astronomy*, Vol. 103, No. 1, 2009, pp. 79–103, doi:10.1007/s10569-008-9169-y.

[25] Circi, C. and Teofilatto, P., "Effect of Planetary Eccentricity on Ballistic Capture in the Solar System," *Celestial Mechanics and Dynamical Astronomy*, Vol. 93, No. 1, 2005, pp. 69–86, doi:10.1007/s10569-005-3640-9.

[26] Neto, E. V. and Prado, A. F. B. A., "Effects of the Eccentricity on the Primaries in the Gravitational Capture Phenomenon," *Advances in the Astronautical Sciences*, Vol. 122, No. 1, 2006, pp. 429–446.

[27] Makó, Z., Szenkovits, F., Salamon, J., and Oláh-Gál, R., "Stable and unstable orbits around Mercury," *Celestial Mechanics and Dynamical Astronomy*, Vol. 108, No. 4, 2010, pp. 357–370, doi:10.1007/s10569-010-9309-z.

[28] Hyeraci, N. and Topputo, F., "The role of true anomaly in ballistic capture," *Celestial Mechanics and Dynamical Astronomy*, Vol. 116, No. 2, 2013, pp. 175–193, doi:10.1007/s10569-013-9481-z.

[29] Makó, Z., "Connection between Hill stability and weak stability in the elliptic restricted three-body problem," *Celestial Mechanics and Dynamical Astronomy*, Vol. 120, No. 3, 2014, pp. 233–248, doi:10.1007/s10569-014-9577-0.

[30] Machuy, A. L., Prado, A. F. B. A., and Stuchi, T. J., "Numerical study of the time required for the gravitational capture in the bi-circular four-body problem," *Advances in Space Research*, Vol. 40, No. 1, 2007, pp. 118–124, doi:10.1016/j.asr.2007.02.069.

[31] Luo, Z. F., Topputo, F., Bernelli-Zazzera, F., and Tang, G. J., "Constructing ballistic capture orbits in

the real Solar System model," *Celestial Mechanics and Dynamical Astronomy*, Vol. 120, No. 4, 2014, pp. 433–450,
doi:10.1007/s10569-014-9580-5.

[32] Luo, Z. F. and Topputo, F., "Analysis of ballistic capture in Sun–planet models," *Advances in Space Research*, Vol. 56, No. 6, 2015, pp. 1030–1041,
doi:10.1016/j.asr.2015.05.042.

[33] Brasil, P. I. O., Prado, A. F. B. A., Deienno, R., and Yokoyama, T., "Study of the gravitational capture of a spacecraft by Jupiter," *Advances in Space Research*, Vol. 55, No. 2, 2015, pp. 668–681,
doi:10.1016/j.asr.2014.11.005.

[34] Russell, R. P. and Lam, T., "Designing ephemeris capture trajectories at Europa using unstable periodic orbits," *Journal of guidance, control, and dynamics*, Vol. 30, No. 2, 2007, pp. 482–491,
doi:10.2514/1.22985.

[35] Luo, Z. F. and Topputo, F., "Capability of Satellite-Aided Ballistic Capture," *Communications in Nonlinear Science and Numerical Simulation*, Vol. 48, 2017, pp. 211–223,
doi:10.1016/j.cnsns.2016.12.021.

[36] Belbruno, E., Gidea, M., and Topputo, F., "Weak stability boundary and invariant manifolds," *SIAM Journal on Applied Dynamical Systems*, Vol. 9, No. 3, 2010, pp. 1061–1089.

[37] Xu, M. and Xu, S. J., "Exploration of distant retrograde orbits around Moon," *Acta Astronautica*, Vol. 65, No. 5, 2009, pp. 853–860,
doi:10.1016/j.actaastro.2009.03.026.

[38] Howell, K. C. and Pernicka, H. J., "Numerical determination of Lissajous trajectories in the restricted three-body problem," *Celestial mechanics*, Vol. 41, No. 1, 1987, pp. 107–124,
doi:10.1007/BF01238756.

[39] Hénon, M., "New Families of Periodic Orbits in Hill's Problem of Three Bodies," *Celestial Mechanics and Dynamical Astronomy*, Vol. 85, No. 3, 2003, pp. 223–246,
doi:10.1023/A:1022518422926.

[40] Russell, R. P., "Global search for planar and three-dimensional periodic orbits near Europa," *The Journal of the Astronautical Sciences*, Vol. 54, No. 2, 2006, pp. 199–226,
doi:10.1007/BF03256483.

[41] Davis, D. C. and Howell, K. C., "Characterization of Trajectories Near the Smaller Primary in the Restricted Problem for Applications," *Journal of Guidance, Control, and Dynamics*, Vol. 35, No. 1, 2012, pp. 116–128,

doi:10.2514/1.53871.

[42] Haapala, A. F. and Howell, K. C., "A Framework for Constructing Transfers Linking Periodic Libration Point Orbits in the Spatial Circular Restricted Three-Body Problem," *International Journal of Bifurcation and Chaos*, Vol. 26, No. 05, 2016, pp. 1630013 1–40, doi:10.1142/S0218127416300135.

[43] Russell, R. P. and Brinckerhoff, A. T., "Circulating Eccentric Orbits Around Planetary Moons," *Journal of Guidance, Control, and Dynamics*, Vol. 32, No. 2, 2009, pp. 424–436, doi:10.2514/1.38593.

[44] Lantoine, G. and Russell, R. P., "Near Ballistic Halo-to-Halo Transfers between Planetary Moons," *The Journal of the Astronautical Sciences*, Vol. 58, No. 3, 2011, pp. 335–363, doi:10.1007/BF03321174.

[45] Lara, M., Russell, R. P., and Villac, B., "Fast estimation of stable regions in real models," *Meccanica*, Vol. 42, No. 5, 2007, pp. 511–515, doi:10.1007/s11012-007-9060-z.

[46] Lantoine, G., Russell, R. P., and Campagnola, S., "Optimization of low-energy resonant hopping transfers between planetary moons," *Acta Astronautica*, Vol. 68, 2011, pp. 1361–1378, doi:10.1016/j.actaastro.2010.09.021.

[47] Campagnola, S. and Russell, R. P., "Endgame Problem Part 2: Multibody Technique and the Tisserand-Poincare Graph," *Journal of Guidance, Control, and Dynamics*, Vol. 33, No. 2, 2010, pp. 476–486, doi:10.2514/1.44290.

[48] Circi, C., "Properties of transit trajectory in the restricted three and four-body problem," *Advances in Space Research*, Vol. 49, No. 10, 2012, pp. 1506 –519, doi:http://dx.doi.org/10.1016/j.asr.2012.02.034.

[49] Baresi, N., Olikara, Z. P., and Scheeres, D. J., "Survey of numerical methods to compute quasi-periodic invariant tori in astrodynamics," *Advances in the Astronautical Sciences*, Vol. 158, 2016, pp. 711–732.

[50] Olikara, Z. P. and Scheeres, D. J., "Numerical method for computing quasi-periodic orbits and their stability in the restricted three-body problem," *Advances in the Astronautical Sciences*, Vol. 145, 2012, pp. 911–930.

[51] Gawlik, E. S., Marsden, J. E., Du Toit, P. C., and Campagnola, S., "Lagrangian coherent structures in the planar elliptic restricted three-body problem," *Celestial mechanics and dynamical astronomy*, Vol. 103, No. 3, 2009, p. 227.

[52] Lara, M. and Russell, R. P., "Computation of a Science Orbit About Europa," *Journal of Guidance,*

Control, and Dynamics, Vol. 30, No. 1, 2007, pp. 259–263, doi:10.2514/1.22493.

[53] Szebehely, V., *Theory of orbits: the restricted problem of three bodies*, Academic Press, New York, 1967.

[54] Broucke, R. A., "Stability of periodic orbits in the elliptic, restricted three-body problem," *AIAA Journal*, Vol. 7, No. 6, 1969, pp. 1003–1009, doi:10.2514/3.5267.

[55] Curtis, H., *Orbital mechanics for engineering students*, Butterworth-Heinemann, 2009.

[56] Robin, I. A. and Markellos, V. V., "Numerical determination of three-dimensional periodic orbits generated from vertical self-resonant satellite orbits," *Celestial Mechanics*, Vol. 21, No. 4, 1980, pp. 395–434, doi:10.1007/BF01231276.

[57] Broucke, R. A., "Periodic orbits in the restricted three-body problem with Earth-Moon masses," *Pasadena, Jet Propulsion Laboratory, California Institute of Technology, 1968.*, Vol. 1, doi:10.2514/3.5267.

[58] Hénon, M., "Numerical exploration of the restricted problem, V," *Astronomy and Astrophysics*, Vol. 1, 1969, pp. 223–238.

[59] Macdonald, M. and McInnes, C., "Spacecraft planetary capture using gravity-assist maneuvers," *Journal of guidance, control, and dynamics*, Vol. 28, No. 2, 2005, pp. 365–369, doi:10.2514/1.11866.

[60] Dutt, P. and Sharma, R., "Analysis of Periodic and Quasi-Periodic Orbits in the Earth–Moon System," *Journal of Guidance, Control, and Dynamics*, Vol. 33, No. 3, 2010, pp. 1010–1017, doi:10.2514/1.46400.

[61] Mazanek, D. D., Merrill, R. G., Brophy, J. R., and Mueller, R. P., "Asteroid redirect mission concept: a bold approach for utilizing space resources," *Acta Astronautica*, Vol. 117, 2015, pp. 163–171, doi:0.1016/j.actaastro.2015.06.018.

[62] Dei Tos, D. A. and Topputo, F., "Trajectory refinement of three-body orbits in the real solar system model," *Advances in Space Research*, Vol. 59, No. 8, 2017, pp. 2117–2132, doi:https://doi.org/10.1016/j.asr.2017.01.039.

[63] Dei Tos, D. A. and Topputo, F., "On the advantages of exploiting the hierarchical structure of astrodynamical models," *Acta Astronautica*, Vol. 136, 2017, pp. 236–247, doi:10.1016/j.actaastro.2017.02.025.